coatings

MDPI

Article

Evaluation of Solid Particle Erosion of EB-PVD TBCs under Thermal Cycling Conditions Based on a Stochastic Approach

Bochun Zhang [1], Kuiying Chen [2,*] and Natalie Baddour [1]

[1] Department of Mechanical Engineering, the University of Ottawa, Ottawa, ON K1N 6N5, Canada
[2] Structures and Materials Performance Laboratory, Aerospace Research Centre, National Research Council Canada, Ottawa, ON K1A 0R6, Canada
* Correspondence: kuiying_chen@hotmail.ca; Tel.: +01-613-993-1247; Fax: +01-613-949-8165

Abstract: The solid particle erosion behavior of electron-beam physical vapor deposition (EB-PVD) thermal barrier coatings (TBCs) was numerically evaluated under thermal cycling conditions. The erosion rates were calculated based on the mechanics-based formulae where the model parameters are fitted to the temperature-process-dependent test data available in the literature. A stochastic approach was applied to simulate the erosion behavior toward service conditions. The mechanics-based formulae were then validated by experimentally measured temperature and sintering-dependent erosion rates from the literature. The pseudoductile erosion behavior is identified for silica particles in the EB-PVD topcoat (TC) erosion system above the intermediate temperatures (~220 °C) due to the softening of partial molten silica particles, thus leading to an increase in the cutting wear and a decrease in deformation wear. The erosion rates are found to decrease versus temperature but increase versus thermal cycles. Such erosion behavior could be attributed to propagation of sintering cracks induced at elevated temperatures. The parametric calculations show that both erosion and thermal cycling parameters have a profound effect on the erosion mechanism of EB-PVD TC. The erosion rate increases at higher solid particle velocity and accumulated mass but displays a pseudoductile erosion behavior versus variation of impacting angles. Two types of erosion mechanisms were evaluated under different thermal cycling conditions. Under the burner cycling test with a short high-temperature dwell period, the erosion mechanism of EB-PVD TBCs is governed by temperature, while under an isothermal cycling test with a high-temperature long dwell period, the erosion is determined by sintering time. The failure mechanisms of EB-PVD TBCs under solid particle erosion processes are discussed combining internal cracking within topcoat and external erosion on the surface of topcoat.

Keywords: solid particle erosion; EB-PVD TBCs; temperature-dependent model parameters; stochastic approach; sintering effect

Citation: Zhang, B.; Chen, K.; Baddour, N. Evaluation of Solid Particle Erosion of EB-PVD TBCs under Thermal Cycling Conditions Based on a Stochastic Approach. *Coatings* **2023**, *13*, 156. https://doi.org/10.3390/coatings13010156

Academic Editor: Charafeddine Jama

Received: 27 October 2022
Revised: 27 December 2022
Accepted: 29 December 2022
Published: 11 January 2023

1. Introduction

Research concerning the failure mechanisms of electron-beam physical vapor deposition (EB-PVD) thermal barrier coating (TBC) systems in the hot section of gas turbine engines have been conducted for several decades [1–8]. Apart from the degradation and damage caused by residual stresses generated via bond coat (BC) oxidation and coefficient of thermal expansion (CTE) mismatch between different coating layers, the hot corrosion of TBCs under high-temperature service environment and solid particle erosion on coating systems were considered as a secondary problem in which the latter is normally described by an impact of external particles on the surface of TBC topcoat (TC) during service period [1,9–14]. The superior durability of EB-PVD TBCs compared to those of atmospheric plasma-sprayed thermal barrier coating systems (APS-TBCs) is partially due to its feathering-like columnar microstructure [15–19]. For solid particle erosion resistance, the columnar boundaries of EB-PVD TBCs have been shown to effectively inhibit crack

propagation induced by the impact of external solid particles [10,12,20]. Under a harsh service environment, it is necessary to investigate the failure mechanism due to solid particle erosion of EB-PVD TBCs. To date, there are a number of test results on erosion rates for EB-PVD TBC versus different erodents at temperatures from room temperature (RT) up to 910 °C [21,22]. Although there are a number of theoretical and numerical models on solid particle erosion of EB-PVD TBCs [10,23–25], these existing modeling results on erosion are mostly qualitative and normally focus on erosion-mechanisms identification, establishing a scaling correlation law between external particle property and erosion test depth along with coating materials' mechanical properties. In the present research, the solid particle erosion and its erosion rate of EB-PVD TBCs are quantified at elevated temperatures for two distinct thermal cycle schemes, i.e., burner cycling and isothermal cycling conditions. By using the temperature, processing and sintering-dependent coating materials' properties, the erosion behavior is described, and soft erosion behavior of particle SiO_2 at high temperature was explained. Furthermore, a stochastic approach was combined with mechanics-based formulae of erosion to evaluate erosion behavior with an aim toward real service working environments, and, finally, explanation on erosion failure was provided by using lateral cracking and sintering cracking induced by solid particle impact.

The present paper is organized as follows. In Section 2, the mechanics-based erosion formulae [26] are introduced and described in detail along with an estimation of erosion and erosion rates versus thermal cycles combining a stochastic approach. In Section 3, model parameters are then fitted to test data considering the effect of temperature variation and time-dependent sintering on erosion rate. The mechanics-based formulae are incorporated to determine the resistance of the target material against erosion, where a stochastic approach is introduced with randomly selected erosion parameters to approximate the erosion rates toward service conditions. In addition, a parametric study is conducted to evaluate the effect of erosion parameters, including impact velocity, accumulated impact mass, impact angle and thermal cycling parameters on erosion rates. In Section 4, which contains the results and discussion, two erosion modes are identified at different stages of thermal cycles versus the ratio of high-temperature dwell time over the total cycling duration. The erosion modes are further correlated to the failure mechanism of EB-PVD TBCs under different thermal cycling conditions. In Section 5, the major conclusions derived from previous sections were summarized.

2. Mechanics-Based Formulae for Evaluating Solid Particle Erosion under Thermal Cycling Environments

Experimentally measured erosion rates for EB-PVD TBCs were tabulated in [21] under various impact angles at selected temperatures. For EB-PVD TBCs, in Ref. [27], the erosion tests were conducted using spherical alumina particles of a diameter of 40 μm at 540 °C with an impact velocity of 122 m/s. In Ref. [22], the erosion tests were carried out using spherical silica particles of a diameter of 60 μm at room temperature (RT) with an impact velocity of 170 m/s and at 910 °C with an impact velocity of 300 m/s. It is evident that the measured erosion rates shown in Table S1 of the Supplementary Materials demonstrate a temperature-dependent behavior. The coatings were eroded in a brittle manner at both RT and 540 °C because the erosion rate increases monotonously with impact angle and the maximum erosion rate was found at the high impact angle (90°), Figures S1 and S2 of the Supplementary Materials. However, the coating was eroded in a pseudoductile manner, according to [22], at 910 °C because the maximum erosion rate was found at an acute impact angle (30°) and then followed a decreasing erosion rate pattern as the impact angle increased, Figures S3 and S4 of the Supplementary Materials. It should be noticed that a pasty deposit of erodent silica was identified on the surface of TC for erosion test conducted at glancing angles at elevated temperatures [22]. This result suggests that during high-temperature erosion processes, there exists a softening and/or partial melting of erodent silica particles upon impinging on the TC surface. The softened silica erodent is capable of pulling out fracture sections of coatings that are otherwise not removed at acute

angles [10,21,22], which consequently results in pseudoductile erosion behavior at elevated temperatures. In the present study, because the erosion rates are calculated under thermal cycling environments, both the brittle and pseudoductile erosion behavior are expected to occur at different stages of thermal cycles.

Neilson et al. [26] proposed mechanics-based formulae in which the total erosion damage is described by accounting for both the cutting wear and deformation wear. The cutting wear is associated with eroding forces parallel to the surface under eroding attack, while the deformation wear is associated with the eroding forces normal to the surface. The kinetic energy of the impacted particles is then divided into two components that are normal and parallel to the target material surface, respectively. During the erosion process, the kinetic energy is absorbed on target material surface and accounts for both cutting wear and deformation wear. Neilson et al. [26] then quantified the cutting wear kinetic energy ϕ and deformation wear kinetic energy ε in terms of releasing a unit mass of eroded material. The formulae of total erosion are described by [26],

$$W_t = \underbrace{\frac{\frac{1}{2}MV^2\cos^2\alpha\sin n\alpha}{\phi}}_{(A)} + \underbrace{\frac{\frac{1}{2}M(V\sin\alpha - K)^2}{\varepsilon}}_{(B)},\ \alpha < \alpha_0 \tag{1A}$$

$$W_t = \underbrace{\frac{\frac{1}{2}MV^2\cos^2\alpha}{\phi}}_{(C)} + \underbrace{\frac{\frac{1}{2}M(V\sin\alpha - K)^2}{\varepsilon}}_{(B)},\ \alpha > \alpha_0 \tag{1B}$$

where

$$n = \frac{\pi}{2\alpha_0} \tag{2}$$

Here, W_t is the total amount of erosion caused by total accumulated mass M of erodent at the attack angle α with the erodent velocity V. In Equation (1), part B accounts for the deformation wear at large angles and parts A and C account for the cutting wear occurring at small angles, respectively [26]. W_t in Equation (1) is calculated versus the attack angle α from the acute angle to the large angle. For small attack angles, the particles may sweep onto the surface and finally leave again with a residual amount of parallel kinetic energy [26]. As the attack angle α increases, there exists a critical angle called α_0 at which the residual parallel component of particle velocity is zero, and then Equations (1A) and (1B) predict the same erosion ($\sin(n\alpha_0) = 1$). For hard materials subject to deformation wear, there also exists a critical impact velocity K below which no erosion damage takes place.

Using the measured erosion rate listed in Table S1 of the Supplementary Materials in Equation (1), the model parameters characterizing the erosion behavior including α_0, n, ε and ϕ are determined, and results are tabulated in Table S2 of the Supplementary Materials at selected temperatures, impact velocity as well as the type of erodent. It is noted that for the term "$\sin(n\alpha)$" (α varies from 0 to α_0) in part A of Equation (1A), the calculated erosion from Equation (1A) is less than that calculated from Equation (1B). In other words, statistically, for a stochastic erosion process with random impact angles, the average erosion rate for a target material with large α_0 is less than that with small α_0, as indicated in the Figure 1 below.

According to Table S2 of the Supplementary Materials, the larger α_0 is obtained at a higher temperature, which indicates that the total erosion rate is smaller than that calculated at RT. This result is in accordance with those from Ref. [28]. Therefore, α_0 is approximated as a quadratic function of temperature given by

$$\alpha_0 = 8.31 \times 10^{-6}T^2 + 0.0082T + 19.47 \tag{3}$$

Here, T is the thermal cycling temperature and is described in Section 3.1, while n is evaluated by substituting Equation (3) into Equation (2).

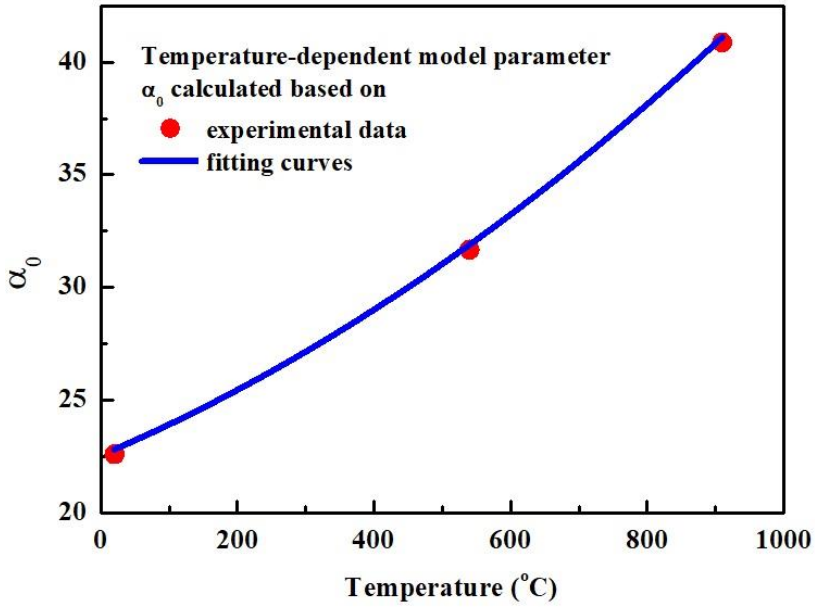

Figure 1. The calculated α_0 versus temperature for EB-PVD TBCs under solid particle erosion.

Unlike the parameters α_0 and n, it is evident that the calculated cutting wear kinetic energy ϕ and deformation wear kinetic energy ε are more dependent on a variation in temperature, as shown in Table S2 of the Supplementary Materials. Hence, in the present study, it is suggested that the cutting wear kinetic energy ϕ and deformation wear kinetic energy ε are governed by multiple factors.

2.1. Parameters Affecting Deformation Wear Kinetic Energy ε

Sheldon et al. [29] studied the plastic deformation of target materials under eroding impact. The impact-induced plastic strain is large enough to exceed the ultimate plastic strain and results in a rupture on the surface of target materials. The authors of [29] demonstrated that the material removed by impacting particles flows out around the sides of the cavity by advancing particle until the displaced material is sufficiently strained to break off [29]. For a spherical particle of a diameter D and density ρ_P that impacts target material with velocity V normal to the surface and the resultant depth q, the erosion amount W removed per gram by impacting particle is proportional to q^3 and is given by [29]

$$W \sim q^3 = \frac{D^3 V^3 (\rho_P)^{1.5}}{H_V^{1.5}} \tag{4}$$

where H_V is the Vickers hardness of the target material.

Considering the erosion generated from a stream of erodent with the accumulated mass M, the deformation wear W_d can be approximated by the mass lost due to impact-removed material as

$$W = \eta \rho_T q^3 \tag{5}$$

where ρ_T is the surface density of target material, and η is a fitting parameter. Substituting Equation (4) into Equation (5) and considering the critical impact velocity K, the deformation wear W_d can be rewritten as

$$W = \eta' \times \rho_T \times \frac{\rho_P \left(\frac{4}{3}\pi R\right)^3 V'^2 V' \sqrt{\rho_P}}{H_V^{1.5}} \tag{6}$$

where $V' = V - K$, and R is the radius of spherical erodent.

To describe the amount of deformation wear with Equation (1) and substituting Equation (6) in part (B) of Equation (1) using $\alpha = 90^{\circ}$, and accumulated total mass $M = \rho_P(4/3\pi R)^3$, the deformation wear kinetic energy ε can be derived as

$$\varepsilon = \eta'' \frac{H_V^{1.5}}{(V-K)\rho_T\sqrt{\rho_P}} \tag{7}$$

where the critical impact velocity K is given by [30]

$$K = \frac{\pi^2}{2\sqrt{10}} \frac{\sigma_y^{2.5}}{\sqrt{\rho_P}} \left[\frac{1-v_P^2}{E_P} + \frac{1-v_T^2}{E_T} \right]^2 \tag{8}$$

E_P and v_P, and E_T and v_T, are elastic moduli and Poisson ratios of erodent and target materials, respectively. Note that the parameters used to describe the properties of the target material in Equations (7) and (8) are temperature-process-dependent, as the erosion rate is evaluated under thermal cycling conditions. Therefore, it is expected that the deformation wear kinetic energy ε varies depending on both temperature and process.

2.2. Parameters Affecting Cutting Wear Kinetic Energy ϕ

As for the approach to evaluating the deformation wear kinetic energy, a similar method is used to evaluate the parameters affecting the cutting wear kinetic energy ϕ. Evans [31] postulated that lateral fracture of ceramic coatings is initiated within a zone that can extend to the elastic–plastic interface under a full penetration. The maximum depth of penetration for spherical indention due to an impact, $Z_{\max}$, is given by [10,21,32] as

$$Z_{\max} = \left(\frac{5\pi\rho_P V^2 k}{4H_V} \right)^{\frac{2}{5}} \left(\frac{R^3}{\sqrt{r}} \right)^{\frac{2}{5}} \tag{9}$$

where k is a constant; r is defined as the radius of the contact point between erodent and target material [10].

For the erosion generated by a stream of erodent with the accumulated mass M, the cutting wear W_c can be approximated by the mass lost due to material removed from impact as

$$W_c = \zeta\rho_T Z_{\max}^3 \tag{10}$$

Here, ζ is a fitting parameter. Substituting Equation (9) into Equation (10), Equation (10) becomes

$$W_c = \xi' \times \frac{\rho_T \times \left(\rho_P \frac{4}{3}\pi R^3\right) \rho_P^{\frac{1}{5}} V^2 (V^2)^{\frac{1}{5}}}{H_V^{\frac{6}{5}}} \times \left(\frac{R}{r}\right)^{\frac{3}{5}} \tag{11}$$

To describe the amount of cutting wear using Equation (1), we substitute Equation (11) in part (A) or part (C) of Equation (1) with $\alpha = 0^{\circ}$ and the total accumulated mass $M = \rho_P(4/3\pi R)^3$. The cutting wear kinetic energy ϕ can be given by

$$\phi = \xi'' \times \frac{H_V^{\frac{6}{5}}}{\rho_T \rho_P^{\frac{1}{5}} V^{\frac{2}{5}}} \times \left(\frac{r}{R}\right)^{\frac{3}{5}} \tag{12}$$

In the present study, under the silica erodent with impact velocities of $V = 170$ m/s and $V = 300$ m/s and an average diameter $2R = 60$ μm, the erosion regime is identified to be the Mode I (erosion-lateral cracking/near-surface plasticity) by using the erosion map [10,12,21], as indicated by the red point in Figure 2, where the lateral cracks are mostly located at the near-surface region as a result of small-particle erosion [8]. By using the erosion map, the radius of the contact point between erodent and target materials

$r \approx 58.51$ μm/s for $V = 300$ m/s and $r \approx 44.23$ μm/s for $V = 170$ m/s is also obtained, respectively.

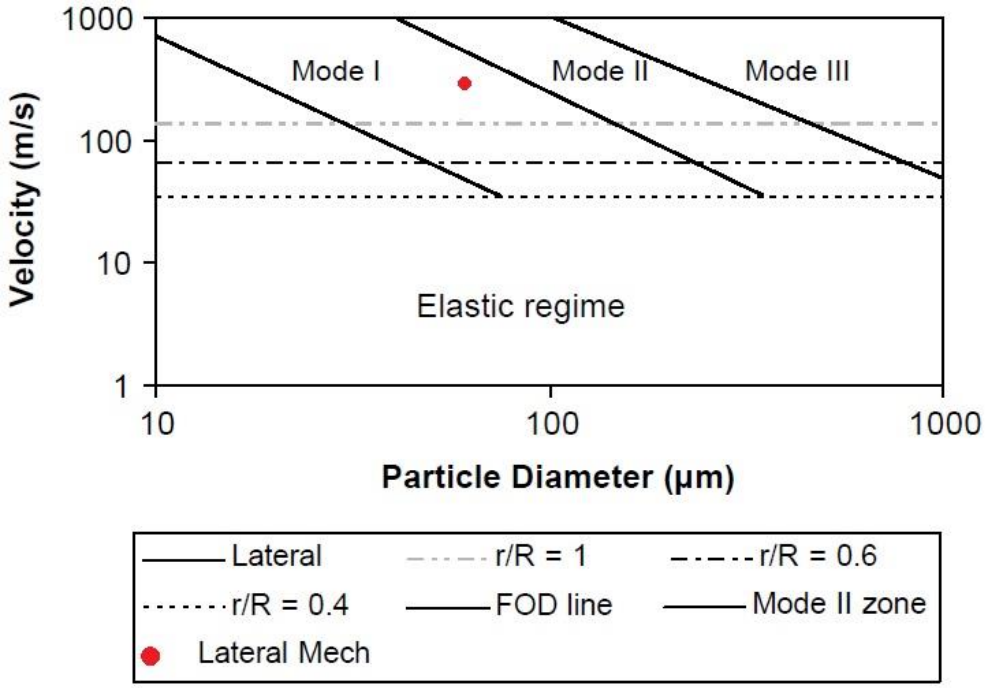

Figure 2. Erosion map for EB-PVD TBCs eroded with silica in which the red spot marks the case for erodent with impact velocity 300 m/s and average diameter 60 μm.

Rewriting Equations (7) and (12) into Equation (13), it should be noted that the term $\left(H_V^n/\sqrt{\rho_P V}\right)^m$ exists for both deformation wear kinetic energy ε and cutting wear kinetic energy ϕ, which indicates that both types of kinetic energies are affected by Vickers hardness, the density of target material and velocity of impacting erodent.

$$\begin{aligned} \varepsilon &= \eta'' \times \frac{1}{\rho_T} \frac{H_V^{\frac{3}{2}}}{\sqrt{\rho_P V}} \\ \phi &= \xi'' \times \frac{1}{\rho_T} \left(\frac{H_V^3}{\sqrt{\rho_P V}} \right)^{\frac{2}{5}} \times \left(\frac{r}{R} \right)^{\frac{3}{5}} \end{aligned} \tag{13}$$

Nevertheless, the difference between the exponent n on Vickers hardness and the overall exponent m suggests its effect of each parameter on kinetic energy for cutting wear and deformation wear processes.

In summary, based on the Supplementary Materials, using the test erosion data listed in Table S1, the erosion rate was fitted to evaluate the erosion model parameters such as the cutting wear kinetic and deformation wear kinetic ε energies. Figure S1 shows the calculated erosion rate of EB-PVD TC under impact of silica particles at RT, and Figure S2 illustrates the calculated erosion rate of EB-PVD TC under impact of alumina particles at 540 °C. While in Figure S3, the test erosion rate at 910 °C was used to obtain the cutting wear kinetic energy ϕ. Using the fitted model parameters, Figure S4 presents the calculated erosion rate of EB-PVD TC under impact of silica particles at 910 °C. It is noted that these fitted model parameters listed in Table S2 will be used to evaluate the solid particle erosion behaviour for EB-PVD TBCs under thermal cycling environments.

Concerning the effect of critical impact velocity K in Equation (8) on deformation kinetic energy, its value was calculated and the result was shown in Figure S5. It shows that the critical impact velocity K has much less effect than the impact velocity applied at either RT (170 m/s) or 910 °C (300 m/s).

Up to date, there are no reliable correlations established that describe complicated interactions between the topcoat stresses with bond coat and substrates under solid particle impact for EB-PVD TBCs; thus, the present paper focuses on investigating the erosion behavior of standing-alone TBC topcoat-YSZ materials rather than the bond coat and substrate. Therefore, this study does not involve interactions such as high temperature on adhesion of coatings to the substrate, changes in the properties of the substrate or an increase in a mismatch between the properties of the substrate and the coating.

2.3. Stochastic Erosion Process for EB-PVD TBCs under Thermal Cycling Conditions

During service operations, the material properties including cutting wear kinetic energy ϕ and deformation wear kinetic energy ε, temperature-dependent n and α_0 differ at each impact event during thermal cycles, which leads to different erosion rates. The erosion rate normally follows a random pattern. Therefore, the erosion rate under thermal cycling conditions is evaluated randomly (corresponding to a random temperature in the thermal cycle) with random impact angles for the given thermal cycles, where a stochastic approach is applied. It is assumed that there are P randomly selected ($P \in [1, 3600]$) impacts occurring at randomly selected times t_i ($I = 1, 2, 3, \ldots P$) within a thermal cycle consisting of a total of 3600 s. For each impact at a random time t_i, the erosion occurs with a random mass, randomly selected impact angle α_i and constant velocity V, as shown in Figure 3.

$$\underbrace{\begin{bmatrix} i=1 \\ t_i = t_1 = 1s \\ m_i = m_1 \\ \alpha_i = \alpha_1 \end{bmatrix}[\ ]\begin{bmatrix} i=2 \\ t_i = t_2 = 3s \\ m_i = m_2 \\ \alpha_i = \alpha_2 \end{bmatrix}\begin{bmatrix} i=3 \\ t_i = t_3 = 4s \\ m_i = m_3 \\ \alpha_i = \alpha_3 \end{bmatrix}[\ ]\ldots\begin{bmatrix} i=P \\ t_i = t_P = 3599s \\ m_i = m_P \\ \alpha_i = \alpha_P \end{bmatrix}[\ ]}_{3600s\ \ for\ \ a\ \ specific\ \ cycle\ \ number\ \ N}$$

Figure 3. The schematic diagram of the stochastic process. 3600 s for a specific cycle number N.

Where [ ] indicates that no erosion occurs at that time point; [i, t_i, m_i, $_i$] indicates it is the ith erosion that occurs at time t_i with impact mass m_i and impact angle α_i. It is then assumed that the accumulated impact mass for a thermal cycle is a constant M, in which

$$M = \sum_{i=1}^{P} m_i \tag{14}$$

For the total accumulated erosion occurring within a specific number of cycles, the total erosion can be calculated by a sum of cutting wear including the components for $\alpha_P < \alpha_0$ and $\alpha_P > \alpha_0$, as well as the deformation wear, as shown in Equation (15).

$$\begin{gathered} W_c = \begin{cases} \sum_{i=1}^{P_A} \frac{\frac{1}{2} m_i V^2 \cos^2 \alpha_i \sin(n(T)\alpha_i)}{\phi} & for\ \alpha_i < \alpha_0 \\ \sum_{i=1}^{P_B} \frac{\frac{1}{2} m_i V^2 \cos^2 \alpha_i}{\phi} & for\ \alpha_i > \alpha_0 \end{cases} \\ W_d = \sum_{i=1}^{P} \frac{\frac{1}{2} m_i (V \sin \alpha_i - K)^2}{\varepsilon} \\ W_t = W_c + W_d \end{gathered} \tag{15}$$

Here, P_A is the total times of impacts with impact angle $\alpha_n < \alpha_0$, and P_B is the total times of impacts with angle $\alpha_n > \alpha_0$ ($P = P_A + P_B$). In addition, the erosion rate W_r (g/Kg) is calculated from

$$W_r = W_t / M \tag{16}$$

The variables that need to be determined stochastically include (a) the total number of impacts P occurring within a specific number of cycles ($P \in [1, 3600]$); (b) the time t_i for erosion occurring at a specific number of cycles ($i = 1, 2, 3 \ldots P$); with (c) the impact mass m_i and (d) the impact angle α_i for erosion at each moment in a thermal cycle. The total number of stochastic simulations for erosion rate calculated at a specific number of cycles is assumed to be 10^6. This number is selected to make sure that there are enough stochastic simulations so that the law of large numbers applies. That is, the average of the results obtained from a large number of trials should be close to the expected value and tends to become closer to the expected value as more trials are performed. With a large number of "sampling calculations", the final erosion rate is found to follow a normal distribution and is calculated with a mean and standard deviation of $\mu + 2\sigma$ using a normal distribution, as will be discussed in Section 4.2.

3. Model Parameters under Thermal Cycles

3.1. Temperature Profile under Thermal Cycling Conditions

As an example of a practical environment for EB-PVD TBCs application, the cycling temperature profile is assumed to consist of a 10-min increase from room temperature (RT) to 1400 °C, a 40-min high-temperature dwell period ($t_{HIGH} = 40$) followed by 10 min of temperature drop. The cyclic temperature field pattern used to describe temperature variations within a thermal cycle was chosen as

$$T = \begin{cases} A_{INC} \times \exp\left(-\frac{t}{W_{INC}}\right) + T_{INC} & 0 < t < t_1 \\ 1673.15 & t_1 < t < t_2 \\ A_{DEC} \times \exp\left(-\frac{t}{W_{DEC}}\right) + T_{DEC} & t_2 < t < t_3 \end{cases} \quad (17)$$

In Equation (17), t_1, t_2 and t_3 represent the time at the end of heating, dwell and cooling processes, respectively. $A_{INC} = -1385.96$, $W_{INC} = 110.11$, $T_{INC} = 1679.11$, $A_{DEC} = 1405.82$, $W_{DEC} = 1405.82$, $W_{DEC} = 150.11$ and $T_{DEC} = 267.33$ are fitting parameters for the heating and cooling process. Following Equation (17), the cycling temperature pattern is fitted by the temperature profile in [33] and is shown in Figure 4.

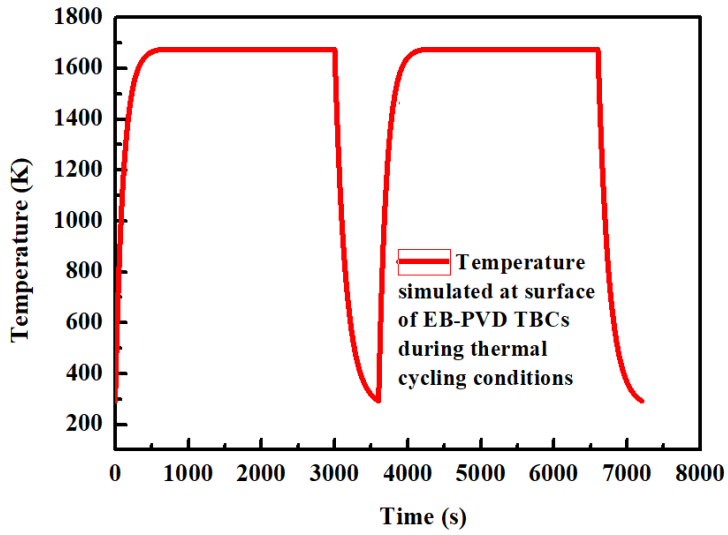

Figure 4. The pattern of surface temperature profile of EB-PVD TBCs (Two thermal cycles) [33].

The effect of high-temperature dwell time on erosion rate is discussed in Section 4, in which different erosion rates are calculated based on variation of the ratio of high-temperature dwell time over the total thermal cycle time, $R_t = t_{HIGH}/t_{cycle}$. The holding time kindly reflects the thermal cycling characteristics. In the present study, two types of thermal cycling are represented by R_t parameter for EB-PVD TBCs erosion. For the burner

cycling test, the holding time is relatively short, with a typical vale of R_t = 0.2, while a large value is selected for the isothermal furnace test with a value of R_t = 0.67.

3.2. Material Properties of EB-PVD TC under Thermal Cycling Conditions

The goal of the current research is to investigate the erosion rate of EB-PVD TBCs under high-temperature thermal cycling conditions. Therefore, the parameters used to evaluate the properties of the target material in Equation (13) are considered to be temperature-dependent, whereas the properties of erodent are obtained from the ambient temperature with a relatively short contact time during the erosion process. Nevertheless, there exists a variety of material properties of erodent relative to the target material in different temperature ranges, reflected by different erosion behavior observed between the low temperature (brittle erosion) and high temperature (pseudoductile erosion). The correlation of material properties between erodent and target material is described using fitting parameters for cutting and deformation wear kinetic energies and will be demonstrated in Section 3.3.

The measured data in [21] showed different types of erodent applied to erosion tests at selected temperatures. Silica particles are chosen to be the erodent against EB-PVD TBCs as the target material for the present study. The parameters of erodent used in Equation (13) are tabulated in Table 1.

Table 1. Parameters of silica erodent at ambient temperatures.

Type of Erodent	Density (Kg/m^3)	Radius of Particle (μm)	Elastic Modulus (GPa)	Poisson's Ratio
SiO_2	2320	60	65.2 [34]	0.17 [34]

The mechanical properties of the target material in Equation (13) include density, Vickers hardness, yield strength and Poisson's ratio used in the analytical expression for critical velocity in Equation (8). The measurement of such mechanical properties was conducted in past research at ambient temperature considering the reinforced method applied in the coating system. In addition to the temperature and time-dependent behavior, it is necessary to point out that these mechanical properties vary versus orientation for anisotropic TC of EB-PVD TBCs.

3.2.1. Variation of the Density of EB-PVD TBCs under Thermal Cycling Conditions

The variation of total relative density ρ_{rl} of topcoat versus sintering time is given by [15]

$$\rho_{rl} = \rho_i + \rho_e - 1 \tag{18}$$

where ρ_i and ρ_e are relative internal (intracolumnar) and external (intercolumnar) densities of YSZ TC. It is assumed that the variation of relative density is only affected by microstructure change, i.e., ρ_{rl} increases due to the sintering at elevated temperature as a consequence of pores shrinking during the high-temperature dwell period [15]. The density of the TC is given by

$$\rho_T = \rho_{dense} \times \rho_{rl} \tag{19}$$

where ρ_{dense} = 5650 kg/m^3 is the density of full dense YSZ [35]. The variation of total density versus cycling time is calculated and illustrated in Figure 5.

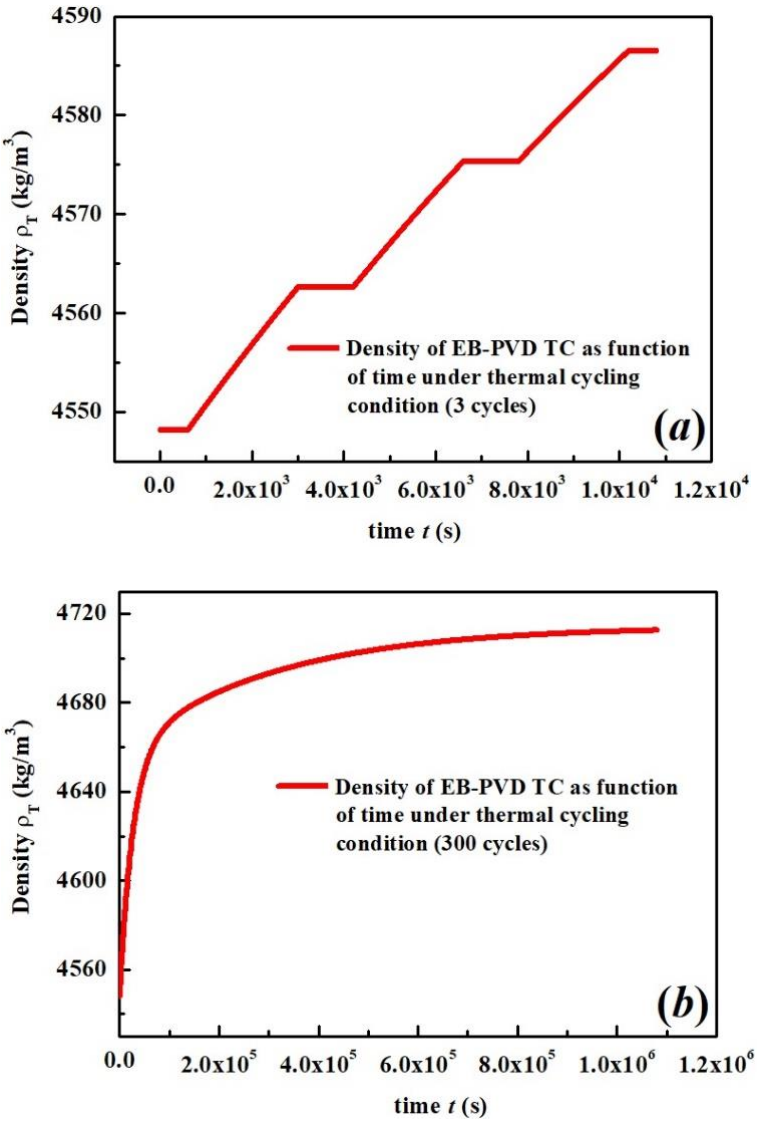

Figure 5. Density of YSZ topcoat versus time (**a**) for the first three cycles and (**b**) full 300 cycles.

3.2.2. Variation of the out-of-Plane Elastic Modulus of EB-PVD TC under Thermal Cycling Conditions

The elastic modulus of the target material is a critical parameter to evaluate the critical velocity of deformation wear in Equation (8). The out-of-plane elastic modulus is used to describe material property of anisotropic TC for EB-PVD TBCs, where the deformation wear kinetic energy in Equation (8) is used to evaluate the resistance of the target material on vertical impact. A method to evaluate the variation of elastic modulus under high-temperature thermal cycling conditions was proposed in [36,37]. Apart from the thermal gradient affecting the TC's sintering behavior, it is assumed in the present study that sintering of EB-PVD Yttria-stabilized Zirconia (YSZ) and the consolidation of the internal pores control TC. These lead to an increase in elastic modulus E_{out} during high-temperature dwell period and are described by [15]

$$E_{out}(t) = \left[1 + \frac{1.5(1-\rho_i)(1-v)(9+5v)}{7-5v}\right]^{-1} E_R \quad (20)$$

Here, ρ_i is the relative internal density of YSZ TC. v is Poisson's ratio v = 0.2, E_R is Young's modulus of fully dense isotropic Zirconia E_R = 210 GPa [38] and t is time. The

calculated elastic modulus as a function of high-temperature dwell time is illustrated in Figure 6.

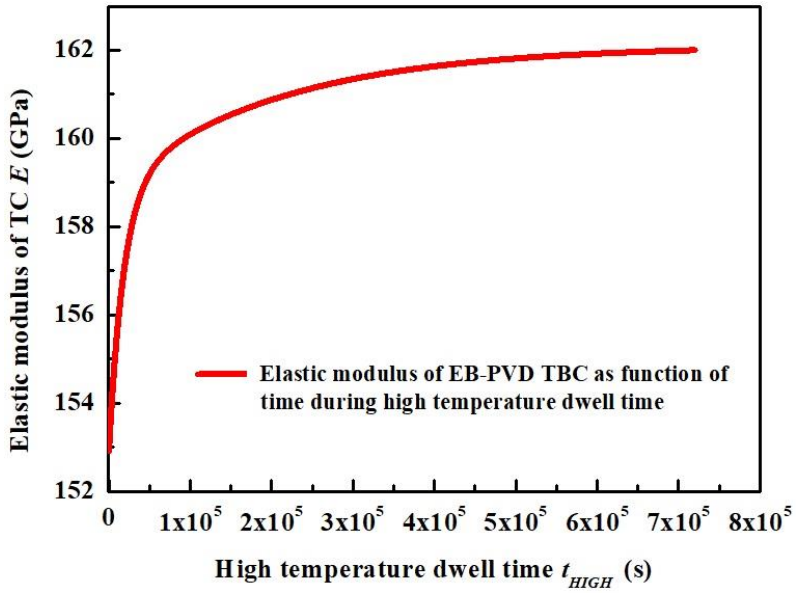

Figure 6. The variation of elastic modulus during high-temperature dwell period due to sintering.

It is difficult to measure elastic modulus during the thermal cycling process. Therefore, in the present study, it is assumed that an increase in elastic modulus during cooling follows the same pattern as that of the elastic modulus upon heating. Additionally, within the dwell period during thermal cycling, elastic modulus is affected by high-temperature sintering. During a thermal cycling period, as the duration of both heating and cooling processes is much shorter than a high-temperature dwell period, the effect of sintering on modulus changes can be neglected for the heating/cooling process [15].

To simulate changes in elastic modulus versus temperature T during thermal cycling, the experimentally measured moduli in [39] are formulated and then fitted approximately by

$$E_{out}(t) = \gamma \exp\left(\frac{\zeta}{T + \varpi}\right) + E_0(t) \tag{21}$$

where γ, ζ and ϖ are fitting parameters with γ = 132.27, ζ = 814.8 K and ϖ = 1574.48 K. $E_0(t)$ is a process-dependent modulus of TC estimated from isothermal sintering at the end of the high-temperature thermal cycle using Equation (20). The temperature-process-dependent elastic modulus can thus be estimated from Equations (20) and (21). The pattern of the out-of-plane elastic moduli versus thermal cycle is shown in Figure 7 for a selected short period. The elastic modulus of the target material under thermal cycling conditions is evaluated by substituting E_{out} as E_T in Equation (8).

3.2.3. Variation of Anisotropic Vickers Hardness of EB-PVD TC under Thermal Cycling Conditions

The Vickers hardness H_V is required in estimating both the cutting wear and deformation wear kinetic energies ε and ϕ in Equation (13). The Vickers hardness H_V in Equation (13) has different values in the in-plane and the out-of-plane directions for anisotropic TC layer of EB-PVD TBCs. The temperature and time-dependent Vickers hardness H_V is evaluated using analytical models. In Ref. [40], the indentation tests were performed at a loading rate of 0.88 mN/s, with a hold period duration of 20 s at a maximum load of 50 mN.

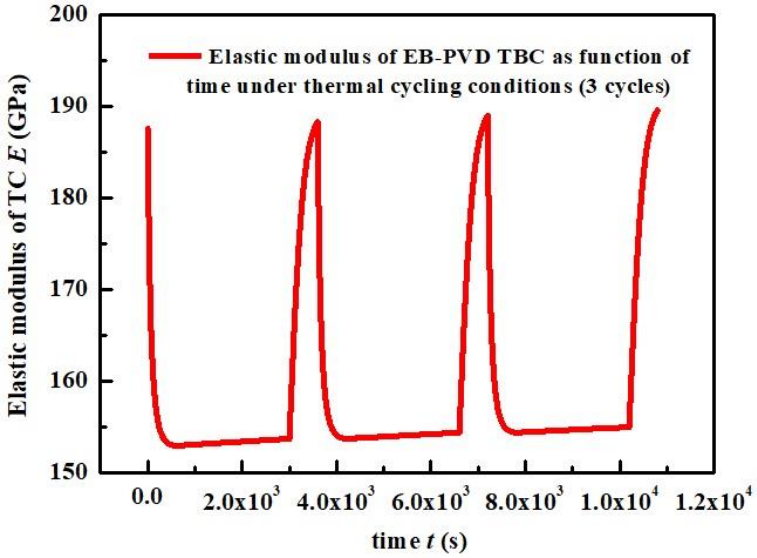

Figure 7. Elastic modulus of YSZ topcoat versus time during the first three cycles.

Similar to the elastic modulus, the time-dependent Vickers hardness H_V is affected by sintering of TC during high-temperature exposure period [41,42]. The intercolumnar cracks disappear from the surface of TC after TBC exposure at 1400 °C [41]. The previous clear columnar structure gap that sintered together during high-temperature dwell time leads to an increase in hardness. The H_V was fitted to experimental data in [41] and is given by

$$H_V^{in}(t) = A_{1H}^{\sin t} \exp\left(-\frac{t}{Q_{1H}^{\sin t}}\right) + A_{2H}^{\sin t} \exp\left(-\frac{t}{Q_{2H}^{\sin t}}\right) + C_{in\_0} \tag{22}$$

$$H_V^{out}(t) = B_{1H}^{\sin t} \exp\left(-\frac{t}{W_{1H}^{\sin t}}\right) + B_{2H}^{\sin t} \exp\left(-\frac{t}{W_{2H}^{\sin t}}\right) + C_{out\_0} \tag{23}$$

$H_V^{in}(t)$ and $H_V^{out}(t)$ are time-dependent Vickers hardness; A_{iH}^{sint}, Q_{iH}^{sint} and C_{in_0} are fitting parameters for the in-plane hardness where B_{iH}^{sint}, W_{iH}^{sint} (i = 1, 2) and C_{out_0} are fitting parameters for the out-of-plane hardness, respectively. The values of fitting parameters are tabulated in Table 2. The calculated Vickers hardness as a function of high-temperature dwell time at 1400 °C is illustrated in Figure 8.

The temperature-dependent cycling Vickers hardness was studied in [43], where the experimentally measured Vickers hardness was obtained through temperature-variant indentation tests for EB-PVD TBCs ranging from room temperature up to 800 °C. To simulate the changes of Vickers hardness versus temperature T during thermal cycling, experimentally measured moduli in [43] are formulated and then fitted approximately as

$$H_V^{in}(T) = A_H^T \exp\left(-\frac{T - 273.15}{Q_H^T}\right) + H_{in\_0}(t) \tag{24}$$

$$H_V^{out}(T) = B_H^T \exp\left(-\frac{T - 273.15}{W_H^T}\right) + H_{out\_0}(t) \tag{25}$$

where $H_V^{in}(T)$ and $H_V^{out}(T)$ are temperature-dependent Vickers hardness; A_H^T, Q_H^T and B_H^T, W_H^T are fitting parameters tabulated in Table 2. $H_{in\_0}(t)$ and $H_{out\_0}(t)$ are the process-dependent hardness of TC estimated from isothermal sintering at the end of high-temperature thermal cycles using Equation (22) and Equation (23), respectively.

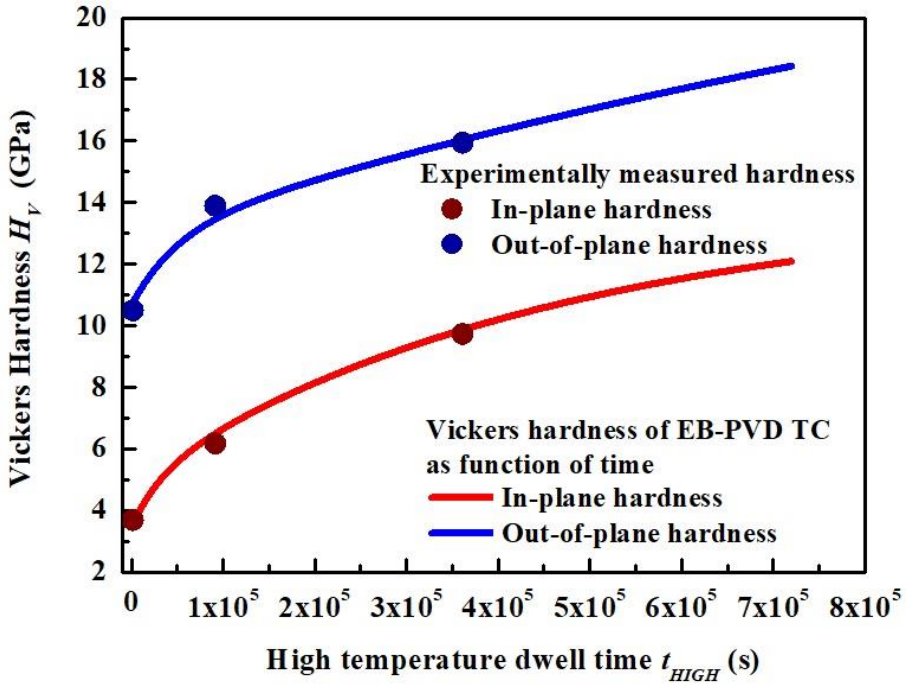

Figure 8. The variation of Vickers hardness during high-temperature dwell period at 1400 °C due to sintering together with experimental data in [40].

Table 2. Fitting parameters used in calculating Vickers hardness.

Fitting Parameters	Values
A_{iH}^{sint}	−8.99942 (I = 1) −1.49089 (I = 2)
$Q_{iH}^{sint}(K)$	126.95095 (I = 1) 9.01642 (I = 2)
$C_{in_0}(GPa)$	13.9525
B_{iH}^{sint}	−14.22029 (I = 1) −2.30728 (I = 2)
$W_{iH}^{sint}(K)$	412.31215 (I = 1) 13.62966 (I = 2)
$C_{out_0}(GPa)$	27.1841
A_H^T	0.31257
$Q_H^T(K)$	332.07745
B_H^T	0.31257
$W_H^T(K)$	332.07745

The assumptions are made that the hardness follows the same pattern on heating as on cooling and that the effect of sintering on hardness can be neglected during this short heating/cooling process. The temperature-process-dependent Vickers hardness can thus be estimated from Equations (22)–(25). The pattern of the out-of-plane elastic moduli versus thermal cycle is shown in Figure 9 for a selected short period. Therefore, the Vickers hardness of the target material under thermal cycling conditions is evaluated by substituting H_V^{in} into the cutting wear kinetic energy ϕ and H_V^{out} into the deformation wear kinetic energy ε, as in Equation (13).

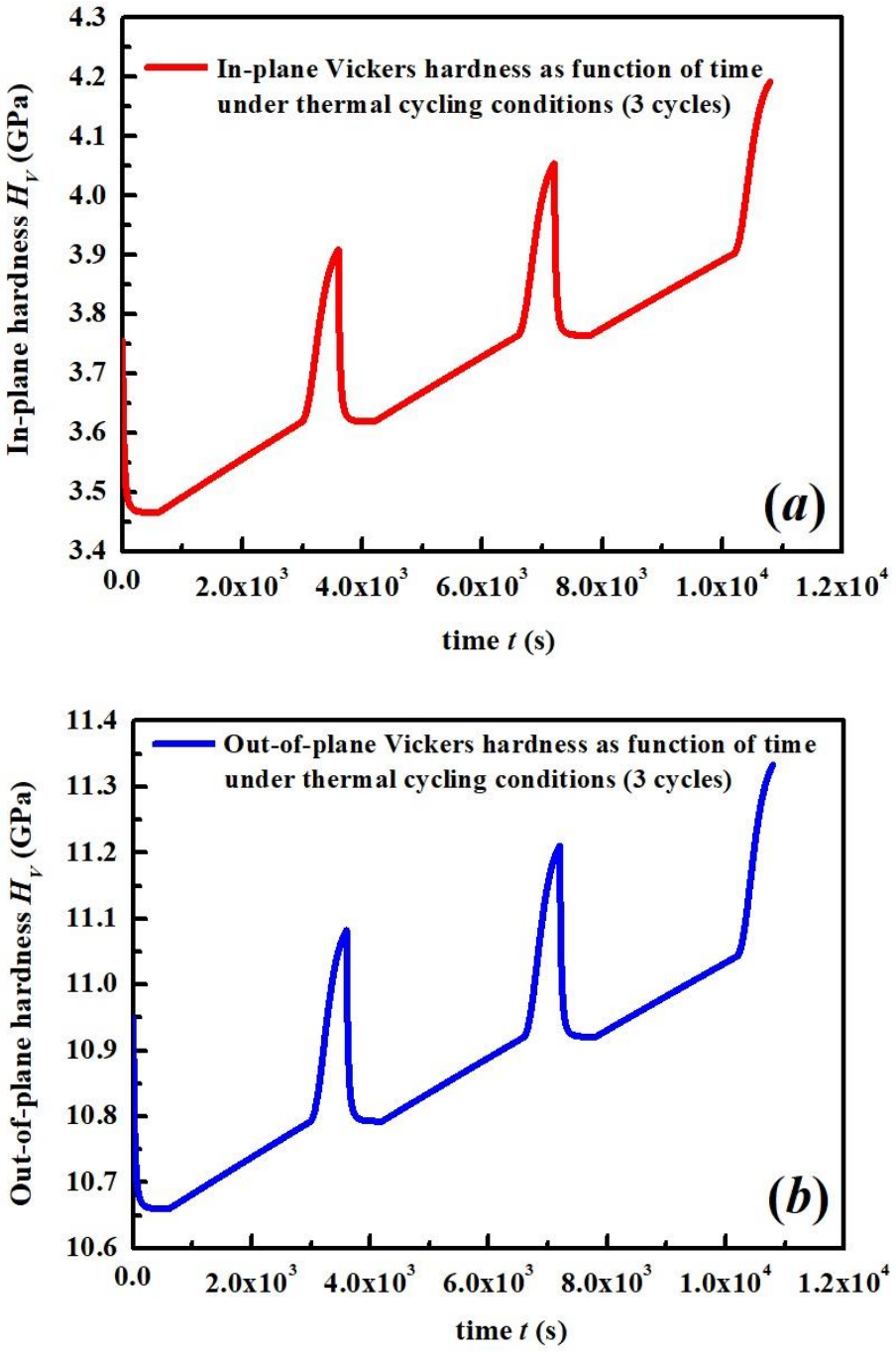

Figure 9. Calculated temperature-process-dependent topcoat hardness for the first three cycles; (**a**) in-plane Vickers hardness; (**b**) out-of-plane Vickers hardness.

3.2.4. Variation of Yield Strength of EB-PVD TC under Thermal Cycling Conditions

The yield strength of the target material plays a significant role in determining the critical velocity for deformation wear in Equation (8). The temperature-dependent yield strength of 7YSZ material was used in [44], where the yield strength decreased as temperature raises. The experimentally measured yield strength with a linear fitting is illustrated in Figure 10.

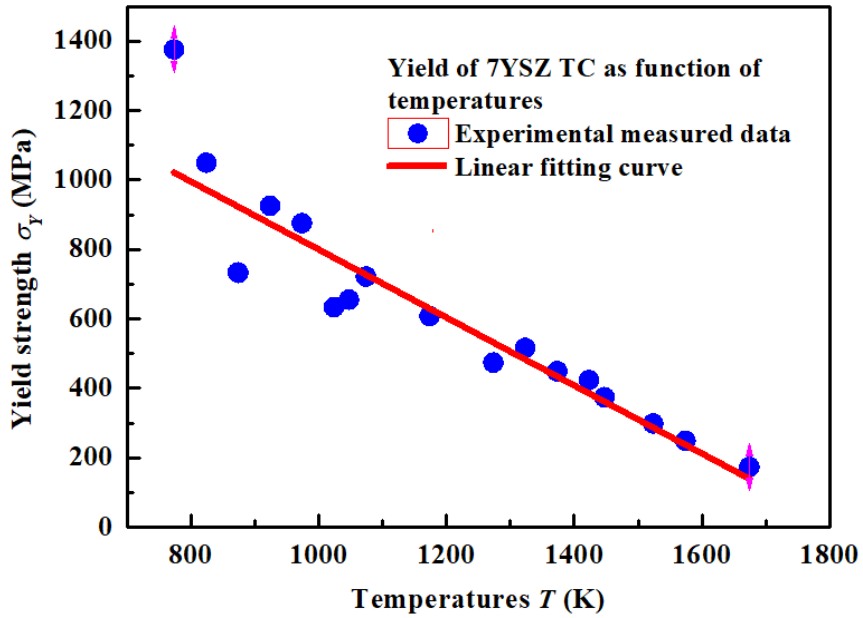

Figure 10. The yield strength of 7YSZ as a function of temperature [44].

In the present study, the sintering effect during high-temperature dwell time leads to a shrinkage of micropores within the columnar structure, which results in an increase in density and yield strength. Therefore, the temperature-process-dependent yield strength of EB-PVD TC is evaluated by Equation (26), associated with the pore closure as a consequence of the sintering at elevated temperatures by

$$\sigma_Y = \frac{\rho_T}{\rho_{dense}} \times (k_Y T + \sigma_{Y0}) \tag{26}$$

where k_Y = –1.029 1/K and σ_{Y0} = 1865.51 MPa are fitting parameters in Figure 10. The density ρ_T is given by Equation (19). The calculated cyclic yield strength and yield strength estimated during high-temperature dwell period are illustrated in Figure 11.

3.3. Characteristics of Cutting Wear and Deformation Wear Kinetic Energies of EB-PVD TC under Thermal Cycling Conditions

Using the temperature-process-dependent parameters determined in the preceding sections, it is possible to evaluate both the cutting and deformation wear kinetic energies versus thermal cycle. The erosion rates were measured at room temperature (RT), 540 and 910 °C [22,27], in which the kinetic energies were calculated as described in Sections SB and SC of the Supplementary Materials via the scheme of Tables S3 and S4. However, the difference in erosion test at these temperatures makes it a challenge to evaluate the target material properties against the erosion process. That is, the type and size of erodent for the erosion test conducted at 540 °C are different from that conducted at RT and 910 °C, in which the impact velocities are different at the three temperatures. Therefore, in the present study, the erosion rates measured at RT and 910 °C are selected to eliminate the effect of erodent type and size on target material properties. The kinetic energies for cutting wear ϕ and deformation wear ε are calibrated by calculating energies at RT and 910 °C and then fitting parameters η'' and ξ'' in Equation (13). Meanwhile, the effect of high-temperature sintering on target materials is further evaluated in kinetic energy, in which the sintering effect introduces potential intercolumnar cracks and further decreases the erosion resistance of the target material.

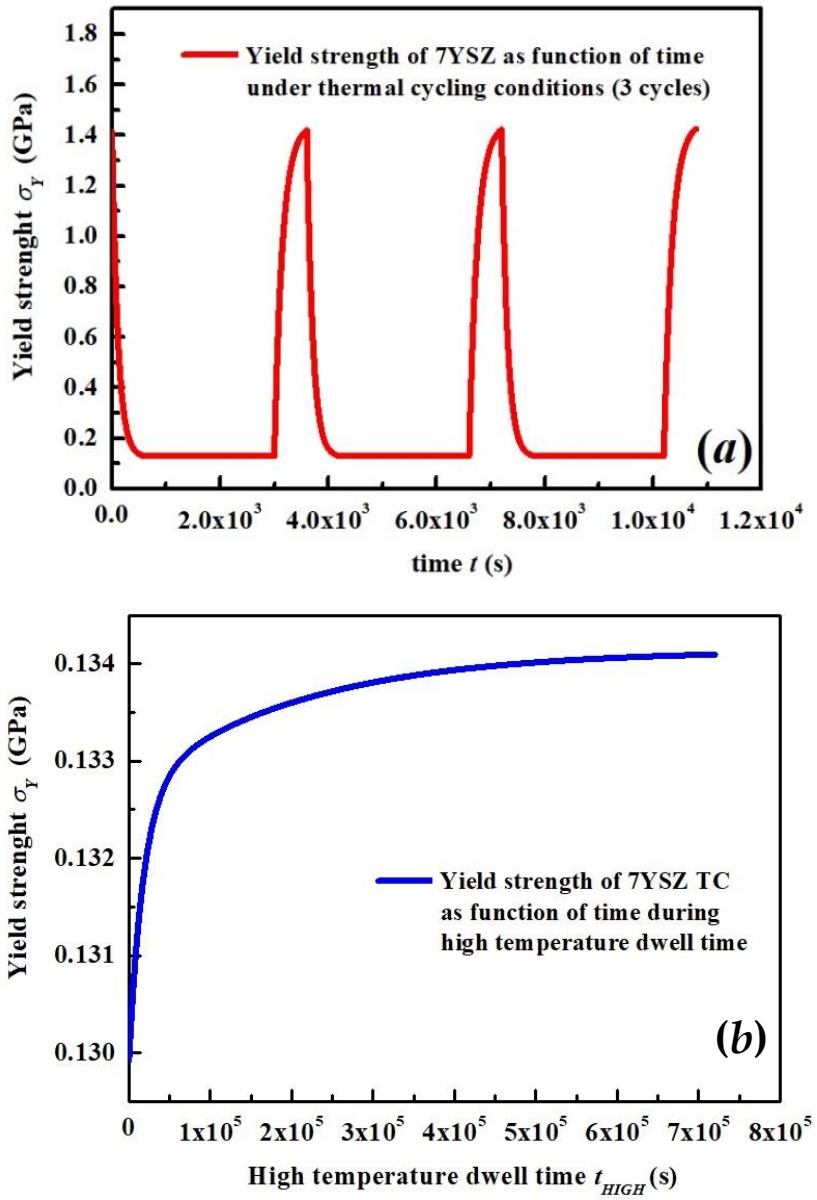

Figure 11. The calculated yield strength of 7YSZ topcoat of EB-PVD TBCs versus time (**a**) for three cycles and (**b**) during high-temperature dwell period.

3.3.1. Fitting Temperature-Dependent Model Parameters η'' and ξ''

To study the effect of the time-dependent sintering on the cutting wear and deformation wear kinetic energies, η'' and ξ'' are fitted at the first thermal cycle using the scheme of Tables S3 and S4. For deformation wear kinetic energy ε, the temperature-dependent fitting parameter can be obtained by substituting the model parameters calculated at both RT and 910 °C for silica erodent into the analytical expression for deformation wear in Equation (13). The calculated results are tabulated in Table 3.

Table 3. The fitted parameters η'' and ξ'' based on deformation wear kinetic energy ϕ and cutting wear kinetic energy ε.

Temperature (°C)	Impact Velocity (m/s)	Deformation Wear Kinetic Energy (m^2/s^2)	Calculated Fitting Parameters η''	Cutting Wear Kinetic Energy (m^2/s^2)	Calculated Fitting Parameters ξ''
20	170	7.90×10^5	0.0289	7.90×10^5	1.3452
910	300	1.17×10^6	910	8.33×10^6	1.0508

In temperatures ranging from RT to 1400 °C during thermal cycling, a linear relationship is assumed between the fitting parameter and temperature to be

$$\eta''(T) = A_\eta \times T(K) + B_\eta \tag{27}$$

where A_η = 0.0005947 and $B_\eta = -0.1454$. Therefore, the temperature-dependent deformation wear kinetic energy is obtained by substituting Equation (27) into Equation (13).

Similarly, for the cutting wear kinetic energy ϕ, the temperature-dependent fitting parameter can be obtained by substituting the model parameters into Equation (13). The calculated results are tabulated in Table 3. In temperatures ranging from RT to 1400 °C during thermal cycling, a linear relationship is assumed between the fitting parameter and temperature to be

$$\xi''(T) = C_\xi \times T(K) + D_\xi \tag{28}$$

where $C_\zeta = -0.0003303$ and $D_\zeta = 1.442$. Therefore, the temperature-dependent cutting wear kinetic energy is obtained by substituting Equation (28) into Equation (13).

3.3.2. Effect of Sintering on Cutting Wear and Deformation Wear Kinetic Energies

Wellman et al. [12,14] revealed that the high-temperature sintering plays a significant role in determining the erosion rate of EB-PVD TBCs. It was suggested that sintering on the surface of the TC during high-temperature dwell time triggers the densification of porous 7YSZ material, which potentially leads to nucleation of sintering cracks, Figure S6 of the Supplementary Materials [45]. These cracks tend to propagate within feathering-like columns at an early stage of TBC lifetime and are stopped by columnar boundaries which act as an inhibitor and potentially decrease the erosion damage by external particles [12,14]. However, as the high-temperature exposure of EB-PVD TBCs proceeds, the vertical gaps and segmentation cracks between the feather columnar structures disappear, whereas the neighbor columns tend to sinter together. This facilitates the nucleation of intercolumnar sintering cracks that propagate parallel to the surface of TC. The formation of intercolumnar cracks between neighbor columns leads to the increase in erosion rates by the impact of external particles on EB-PVD TC [12,14]. In addition, the excessive erosion process will lead to a significant decrease in erosion resistance [13], which facilitates the erosion process of EB-PVD TBCs. Therefore, it is necessary to incorporate the effect of sintering cracks on kinetic energies in order to evaluate the sintering on time-dependent thermal cycling erosion behavior. This behavior is described mathematically by Equation (29),

$$\begin{aligned} \varepsilon(T,t) &= \varepsilon(T) \times \tfrac{1}{f(a)} \\ \phi(T,t) &= \phi(T) \times \tfrac{1}{g(a)} \end{aligned} \tag{29}$$

where a is the sintering crack length, and $\varepsilon(T,t)$ and $\phi(T,t)$ are temperature-process-dependent deformation wear and cutting wear kinetic energies, respectively. The effect of sintering cracks on the decrease in deformation wear kinetic and cutting wear kinetic energies is described by $f(a)$ and $g(a)$, Equation (30). Using Table S3 of the Supplementary Materials, the fitting parameters are obtained from experimentally measured erosion rates as a function of sintering time at different elevated temperatures [12], and results are tabulated in Table 4.

The details of the modeling process are described in Section SB, and model calibration is described in Section SC in the Supplementary Materials.

$$f(a) = A_{crack} \times \exp\left(\frac{a}{Q_{crack}}\right) + y_{\varepsilon}$$
$$g(a) = B_{crack} \times \exp\left(\frac{a}{W_{crack}}\right) + y_{\phi} \quad (30)$$

Table 4. Fitting parameters used in calculating kinetic energies.

Fitting Parameters	Values for V = 300 m/s	Values for V = 170 m/s
A_{crack}	9.14166×10^{-4}	1.34675×10^{-7}
Q_{crack}	−3.73973	−1.20293
y_{ε}	0.62356	0.70749
B_{crack}	2.76605×10^{-6}	6.64357×10^{-7}
W_{crack}	−1.96022	−0.50085
y_{ϕ}	0.60787	0.69595

The through-thickness fracture toughness and its growth behaviour normally vary with respect to the crack length [46–49] as illustrated in Figure S7 in the Supplementary Materials. This correlation of fracture toughness against crack length is then used to evaluate on the behaviour of $f(a)$ and $g(a)$ in Equation (30) to study their effect on both the cutting and deformation wear kinetic energies.

Substituting Equation (30) into Equation (29) gives the temperature-process-dependent cutting wear kinetic energy ϕ and deformation wear kinetic energy ε. The calculated results at impact velocity V = 300 m/s are demonstrated in Figure 12. Similar calculated results are obtained at impact velocity V = 170 m/s but with higher magnitudes of cutting wear and deformation wear kinetic energies since the lower velocity is used in Equation (13).

According to Figure 12a,b, both kinetic energies decrease versus time, which indicates that more erosion is expected with TBCs under longer sintering periods. Meanwhile, the calculated results indicate that deformation wear kinetic energy increases and cutting wear kinetic energy decreases when temperature increases. Based on experimental data, an explanation for the calculated temperature-dependent kinetic energies is given below.

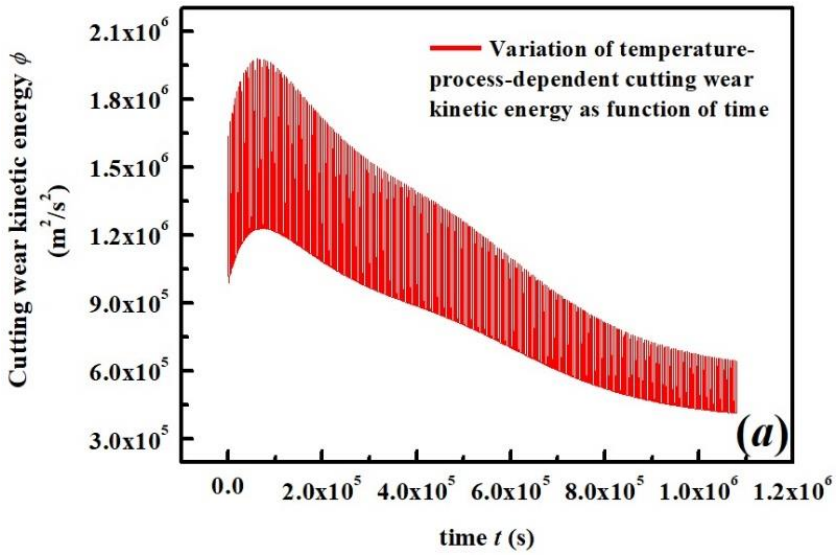

Figure 12. *Cont.*

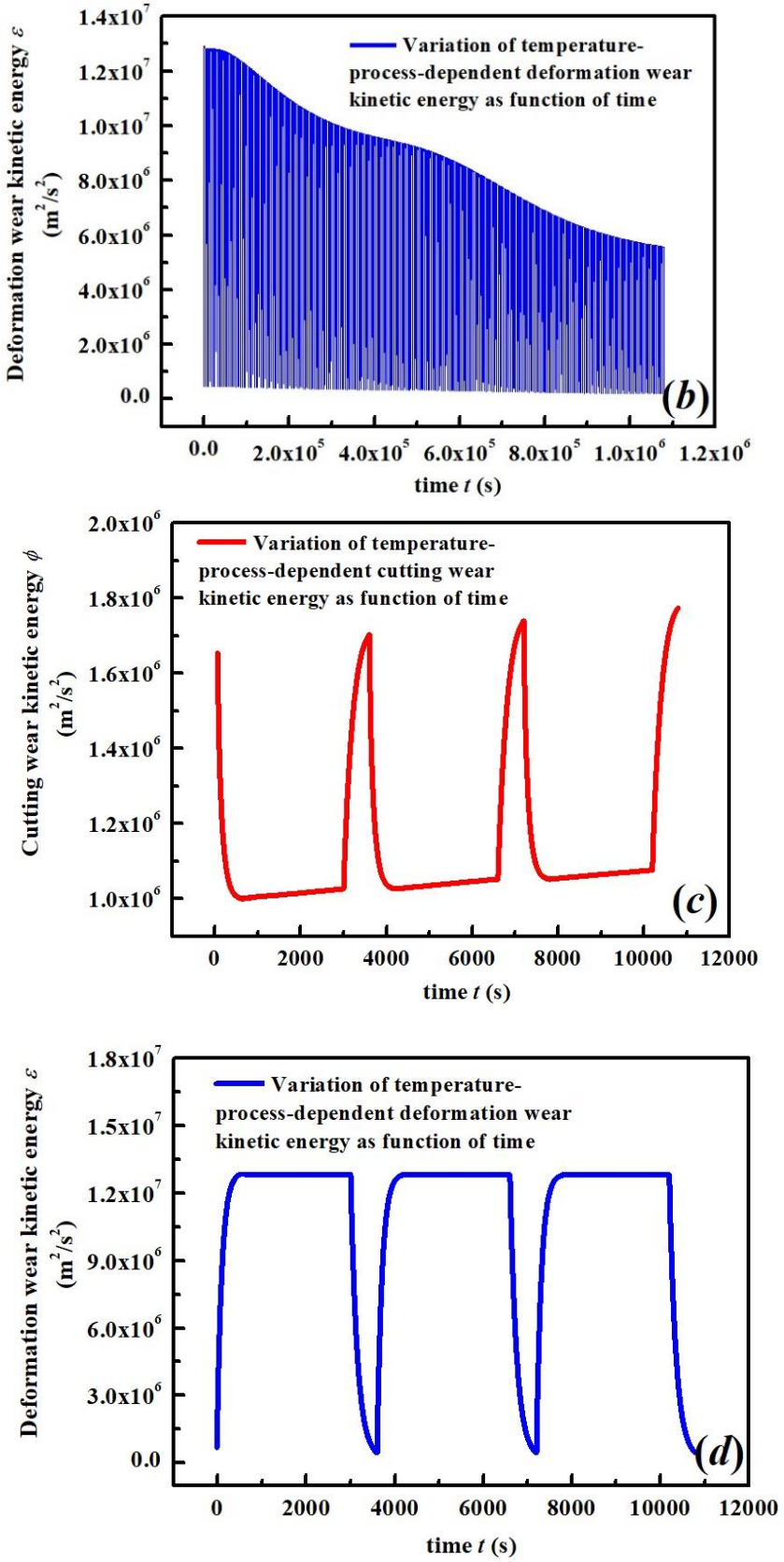

Figure 12. The variation of kinetic energy at V = 300 m/s versus time, (**a**) cutting wear in a full cycle, (**b**) deformation wear in a full cycle, (**c**) cutting wear with three cycles and (**d**) deformation wear with three cycles.

The maximum erosion rates identified at acute angles at elevated temperatures were described in [10,21,22]. Softening/partial melting/pasty of erodent silica particles do more damage at glancing angles according to the erosion data at 910 °C tabulated in Table S1 of the Supplementary Materials. This may suggest an increase in cutting wear, corresponding to a decrease in cutting wear kinetic energy as temperature increases. This softening of erodent could also explain the temperature-dependent deformation wear kinetic energy, which corresponds to a decrease in erosion rate at large impact angles at elevated temperatures. The experimentally measured erosion rates at 90° for EB-PVD TC are tabulated in Table 5 [21].

Table 5. The experimentally measured erosion rates at an impact angle of 90° for EB-PVD TC versus temperature [21].

Temperature (°C)	Erodent	Impact Velocity (m/s)	Erosion Rates (g/kg)	Erodent	Impact Velocity (m/s)	Erosion Rates (g/kg)
RT	40 μm alumina particles	/	/	60 μm silica particles	170	17.4
540		122	14.7		/	/
705			25.0			
815			25.6			
910		/	/		300	5.4

It is evident that for silica erodent, deformation wear determined by erosion rate measured at large angles drops dramatically at elevated temperatures, even if a higher impact velocity was applied. Note that the erosion rate of EB-PVD TBCs under alumina particle attack increases versus temperature, which is opposite to that of silica erodent. In the present study, it is considered to treat the erodent and target material as a system, i.e., the cutting/deformation kinetic energy must be evaluated by considering the temperature-dependent material properties of both the coating system and erodent. For a silica particle–EB-PVD TC erosion system, while a softening/half-melting silica particle impacts the surface of EB-PVD TC (silica softens at 500 °C [50]) at high temperature at large angles, it is possible that a partial melting silica erodent remains at the surface of target materials, which reduces the actual measured erosion rates. This further leads to a decrease in the calculated deformation wear and a corresponding increase in deformation wear kinetic energy versus temperature. On the other hand, for an alumina particle–EB-PVD TC erosion system, it is possible that erosion rates measured at elevated temperatures reveal the actual deformation wear, considering that the alumina particles are more heat-resistant and unlikely to be stuck on the surface of TC. This explains the increasing erosion rates as temperature increases in Table 5. Nevertheless, it is reasonable to consider that the variation of cutting/deformation wear at elevated temperatures reveals the effect of different thermophysical properties of erodent on erosion rate of the target material, which is revealed by temperature-dependent fitting parameters $\eta''(T)$ and $\xi''(T)$ in evaluating the kinetic energy.

4. Results and Discussion

The calculated erosion W_C and erosion rate W_r under thermal cycling conditions are presented in the present section. A parametric study is conducted to evaluate the effect of impact velocity, impact angles and accumulated erodent mass on the erosion rate versus the number of thermal cycles. The effect of ratio R_t of high-temperature dwell time over the total time of the thermal cycle on the erosion rate is also discussed.

4.1. Temperature-Time-Dependent Erosion Rate during Thermal Cycling Versus Erosion Parameters

Based on the determined temperature-process-dependent model parameters, the current mechanics-based formulae can be used to predict the erosion and erosion rate of silica particle–EB-PVD TC erosion systems under thermal cycling combining a stochastic approach. As described in Section 2.3, considering the randomly determined (a) total number of impacts *P,* (b) time t_i for erosion at a specific number of cycles with (c) impact mass m_i and (d) impact angle α_i for erosion at each moment of a thermal cycle as an independent event, the erosion and erosion rate can be estimated by statistical methods based on a massive number of repeated independent experiments. The calculated erosion rate is shown to follow a normal distribution pattern with a mean value and standard deviation $\mu \pm 2\sigma$ based on the 68-95-99.7 rule. An example is given in Figure 13 that shows the calculated erosion rates at the 10th cycle with impact velocities of 300 and 170 m/s, respectively.

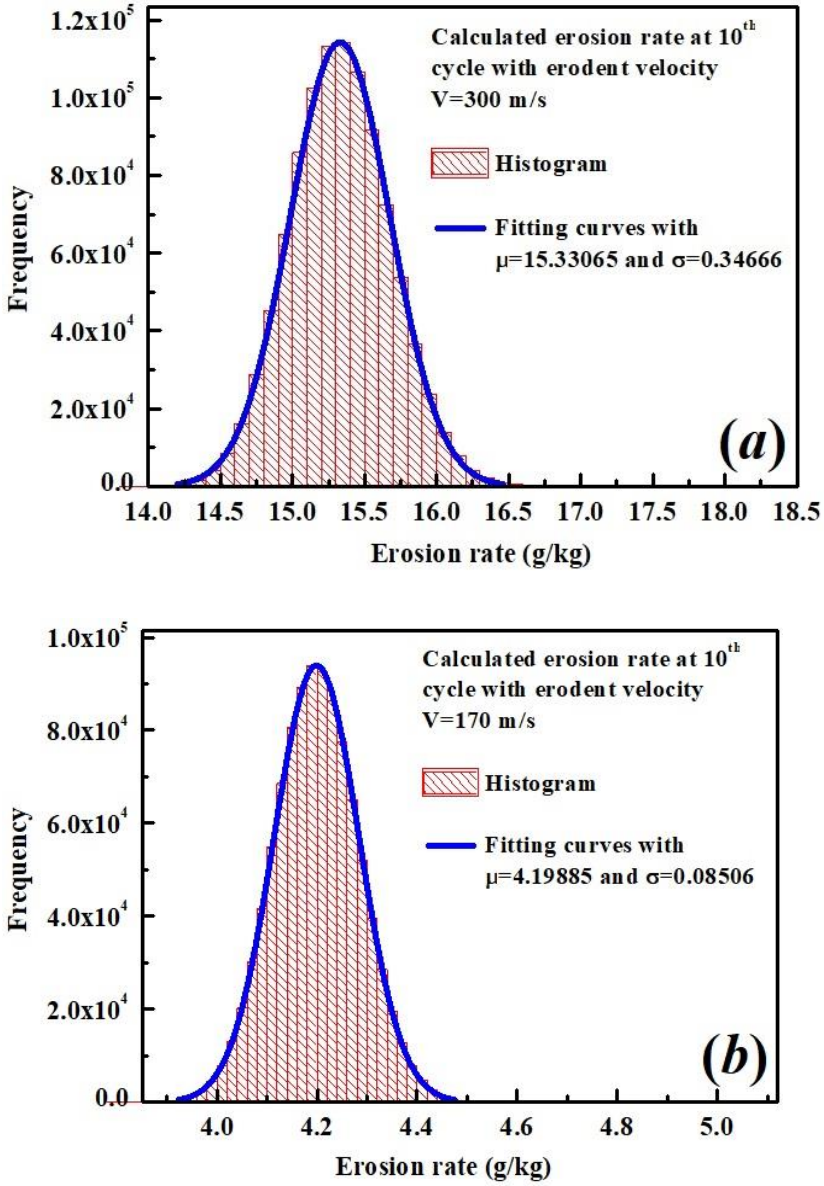

Figure 13. The calculated erosion rate at 10th cycle with impact velocity (**a**) V = 300 m/s (**b**) V = 170 m/s.

4.1.1. The Calculated Erosion Rate vs. Thermal Cycle and Impact Velocity

The effect of impact velocity on erosion rate is evaluated using the parameters in Table 6. The calculated erosion rates are illustrated in Figure 14 versus thermal cycles at two different impact velocities.

Table 6. Parameters used to calculate erosion rates under different impact velocities.

No# of Cycle	Temperatures (°C)	Impact Angles (°)	Impact Mass (kg)	Impact Velocity (m/s)
Determined cycle number N ranging from [10, 300]	Randomly selected T ranging from [RT, 1400]	Randomly selected α ranging from [5, 90]	Randomly selected m_i ranging from [0, M]	Determined V: 170,300

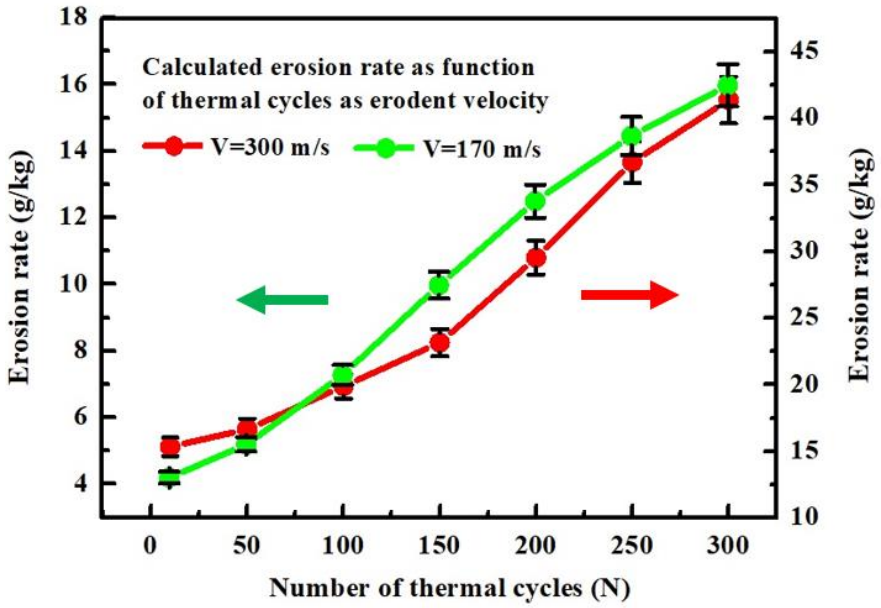

Figure 14. The calculated erosion rate versus thermal cycles at impact velocities V = 300 m/s and V = 170 m/s.

It is evident that both erosion rates increase versus thermal cycles, and normally large impact velocity results in a heavy erosion. A particle with a larger impact velocity generates larger kinetic energy (Equation (15)), and cutting wear/deformation wear kinetic energy decrease as impact velocity increases. In addition, larger impact velocity may lead to the propagation of sintering cracks, which potentially results in propagation of delamination cracks due to the erosion impact.

4.1.2. The Calculated Erosion Rate versus Accumulated Erodent Mass under Thermal Cycles

The effect of accumulated mass on erosion is discussed based on parameters tabulated in Table 7. The erosions are calculated versus accumulated mass ranging from 1g to 1 kg at various stages of thermal cycles, as shown in Figure 15.

Table 7. Parameters used to calculate erosion rates under different impact velocities.

No# of Cycle	Temperatures (°C)	Impact Angles (°)	Impact Mass (g)	Impact Velocity (m/s)
Determined cycle number N ranging from [10, 300]	Randomly selected T ranging from [RT, 1400]	Randomly selected α ranging from [5, 90]	Determined accumulated mass M ranging from [10, 1000]	Determined V: 300

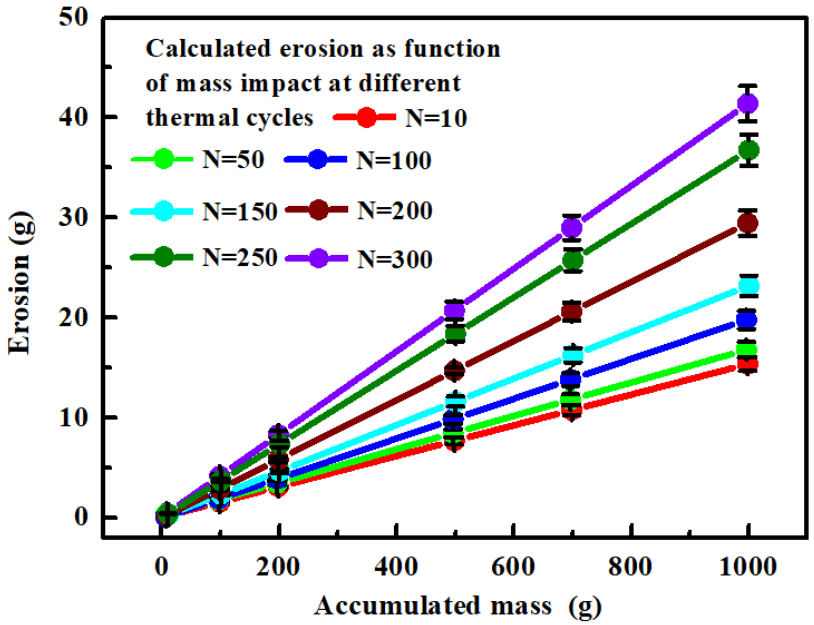

Figure 15. The calculated erosion versus accumulated mass at selected thermal cycles.

It is evident that a linear relationship is obtained for erosion versus accumulated mass, in which the erosion rate (slope of curves) is constant. For erosion calculated at different stages of thermal cycles, it is suggested that the growth of sintering cracks plays a significant role in lowering the magnitude of kinetic energies, as shown in Figure 12, which results in higher erosion estimated at later stages of thermal cycles.

4.1.3. The Calculated Erosion Rate versus Impact Angles under Thermal Cycles

The effect of impact angles on erosion is discussed based on the parameters used and tabulated in Table 8. The erosion rates are calculated versus impact angles ranging from 5° to 90° at various stages of thermal cycles, as shown in Figure 16.

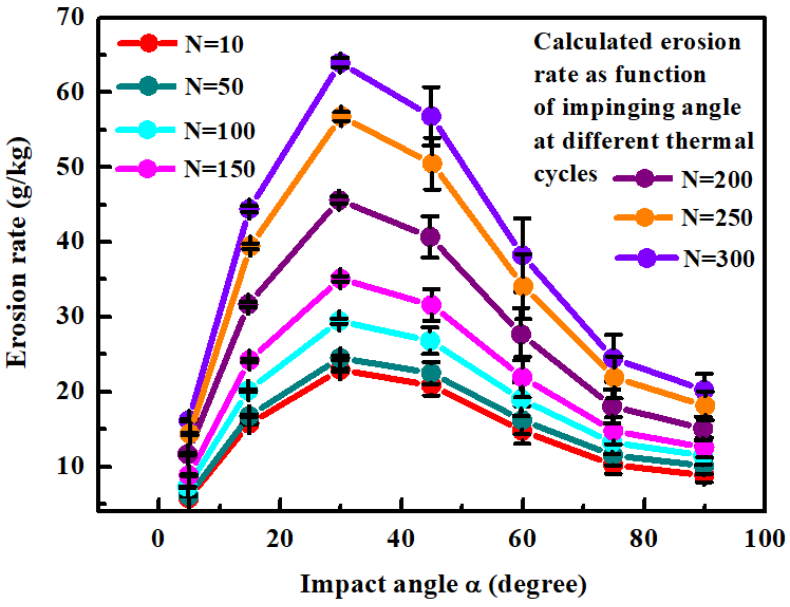

Figure 16. The calculated erosion rate versus impact angle α at selected thermal cycles.

Table 8. Parameters used to calculate erosion rates at different impact angles.

No# of Cycle	Temperatures (°C)	Impact Angles (°)	Impact Mass (kg)	Impact Velocity (m/s)
Determined cycle number N ranging from [10, 300]	Randomly selected T ranging from [RT, 1400]	Determined impact angles α ranging from [5, 90]	Randomly selected m_i ranging from [0, M]	Determined V: 300

Because of propagation of sintering cracks as shown in Figure S8 of the Supplementary Materials, the erosion rate calculated at later stages of thermal cycles is higher than that estimated from earlier stages. This is reflected by an increase in peak erosion rates, estimated at 30° as the thermal cycle proceeds. In addition, all the erosion curves estimated versus impact angle suggest that erosion of EB-PVD TC under thermal cycling occurs in a pseudoductile erosion manner. This is correlated to erosion behavior under elevated temperatures. In the present work, it is expected that the pseudoductile erosion may be estimated at temperatures above 220 °C, as shown in Figure S9 of the Supplementary Materials. Statistically, the probability for erosion occurring during high-temperature dwell time equals the ratio $R_t = 2/3$. Therefore, a relatively large probability of erosion occurs at elevated temperatures, making the cyclic erosion pseudoductile, where the sintering leads to an increase in the maximum erosion rate calculated at glancing angles.

4.2. Temperature-Time-Dependent Erosion Rate during Thermal Cycling Based on Variation of Thermal Cycling Parameters

Apart from the effect of erosion parameters on erosion (rates), the parameters controlling the thermal cycling conditions may also affect erosion behavior of EB-PVD TC. To date, two different thermal cycling tests were conducted in examining the performance of EB-PVD TBCs. The first is an isothermal furnace test, which consists of a slow heating/cooling period with a relatively long high-temperature dwell time. This facilitates the propagation of sintering cracks at elevated temperatures [1,4,36,37]. The second is a burner cycling test (burner rig test), which consists of rapid heating and cooling periods, but with a relatively short high-temperature dwell time. This is used to simulate a process of subsonic engine takeoff and shutdown in real service conditions [33,51–53]. Irrespective of the effect of temperature change rate on erosion behavior, it is expected that the ratio R_t will have a significant effect on erosion behavior of EB-PVD TC. This is evaluated and described in the following sections.

4.2.1. The Calculated Erosion Rate Versus Ratio R_t

According to Figure S9 of the Supplementary Materials, the calculated erosion rate decreases as temperature increases due to the overall increase in temperature-dependent kinetic energies. The propagation of sintering cracks during high-temperature dwell time facilitates erosion at elevated temperatures, which results in an overall increase in erosion rates at later stages of thermal cycles (Figures 14–16). It appears that two opposite mechanisms dominate the high-temperature erosion behavior of EB-PVD TC. The results illustrated in Figure S9 of the Supplementary Materials only consider the erosion rates estimated during temperature variation at the first cycle, without involving factors such as sintering time-dependent parameters. To investigate the effect of high temperature on erosion of EB-PVD TC, it is necessary to estimate the erosion rate versus the ratio R_t.

The effect of high-temperature dwell time on erosion is discussed based on parameters tabulated in Table 9. The erosion rates are calculated versus the ratio R_t from 0.2 to 0.67 at various stages of thermal cycles in Figure 17.

Table 9. Parameters used to calculate erosion rates at selected high-temperature dwell period.

No# of Cycle	Temperatures (°C)	Impact Angles (°)	Impact Mass (kg)	Impact Velocity (m/s)	Ratio of R_t=t_{HIGH}/t_{cycle}
Determined cycle number N ranging from [10, 300]	Randomly selected T ranging from [RT, 1400]	Randomly selected α ranging from [5, 90]	Randomly selected m_i ranging from [0, M]	Determined V: 300	Determined R_t ranging from [0.2, 0.67]

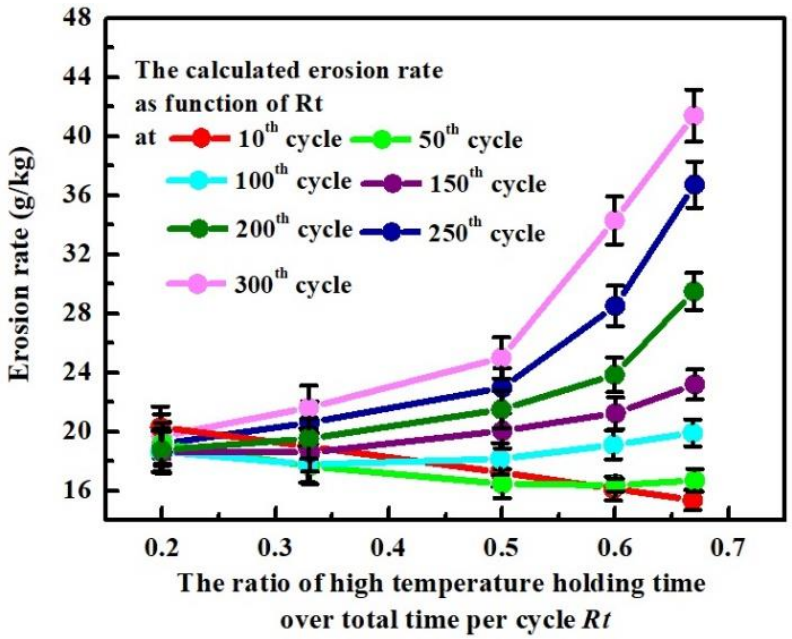

Figure 17. The calculated erosion rate versus the ratio R_t.

Two different erosion modes are identified with respect to different stages of thermal cycles. It is evident that at an early stage of thermal cycles, the erosion behavior is dominated by temperatures, i.e., the longer the high-temperature dwell time (so the higher the ratio R_t), the higher the probability that erosion occurs at elevated temperatures. As the sintering crack is inhibited at the early stages of thermal cycles, the estimated erosion rates follow the results indicated by the red curve in Figure 17, where the overall erosion rates decrease as high-temperature dwell time increases. At the later stage, the erosion behavior is dominated by the sintering of TC, i.e., sintering of TC at later stages of thermal cycles results in sintering cracks reorienting at deeper planes away from the surface of TC, Figure S8 of the Supplementary Materials. This in turn may further lead to a larger amount of fractured TC pulled out under cutting wear at glancing angles, thus leading to an increased erosion rate.

Figure S10a illustrates the ratio of cutting wear over deformation wear versus impacting angles at selected temperatures, in which the erosion is dominated by cutting wear at shallow angles with an increase in deformation wear as the impact angles increase. It is also found in Figure S10b that the ratio of cutting wear over deformation wear is higher at elevated temperatures compared to that at lower temperatures, which can be explained by softening/partially melting/pasty of silica erodent capable of pulling out fractured sections of coating that otherwise cannot be removed at shallow angles [10,13,21].

Using Table S4 of the Supplementary Materials, Figure S11 illustrates the calculated erosion rates for EB-PVD TC under various presintering treatments under different temperatures, together with experimentally measured erosion [12,54,55].

4.2.2. The Calculated Erosion Versus Accumulated Erodent Mass under Different Ratio R_t

The erosion was further validated by erosion rate estimated versus the accumulated mass, with selected ratios R_t at selected stages of thermal cycles, Table 10. The calculated erosion is shown in Figure 18 considering the ratio R_t from 0.2 and 0.67.

Table 10. Parameters used to calculate erosion rates versus accumulated mass with selected high-temperature dwell period and thermal cycles.

No# of Cycle	Temperatures (°C)	Impact Angles (°)	Impact Mass (g)	Impact Velocity (m/s)	Ratio of R_t=t_{HIGH}/t_{cycle}
Determined cycle number N = 10,300	Randomly selected T ranging from [RT, 1400]	Randomly selected α ranging from [5, 90]	Determined accumulated mass M ranging from [10, 1000]	Determined V: 300	Determined R_t = 0.2, 0.67

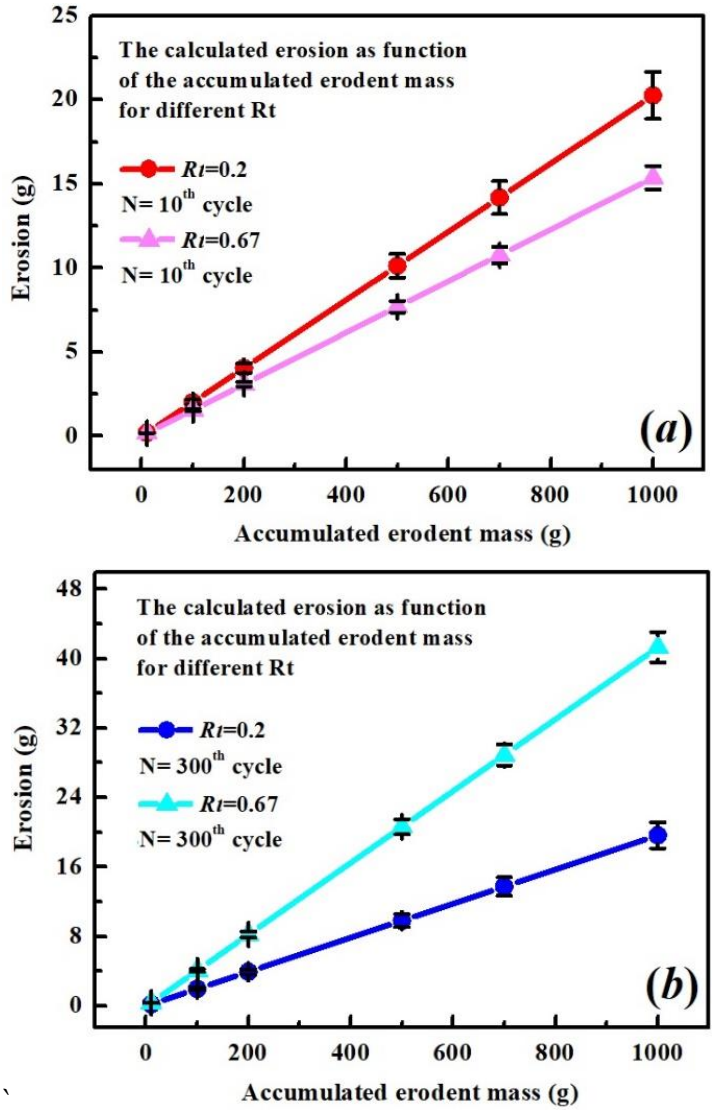

Figure 18. The calculated erosion versus accumulated mass with selected ratios R_t at specific stages of thermal cycles; (**a**) N = 10, (**b**) N = 300.

According to Figure 18a, higher erosion is obtained with a lower ratio R_t, which indicates temperature-dependent erosion at the early stages of the thermal cycles. In

Figure 18b, higher erosion is obtained from a higher ratio R_t when the propagation of sintering cracks facilitates further erosion at later stages of the thermal cycles. Note that the difference between the two curves in Figure 18a is smaller than that obtained in Figure 18b. This could suggest that the effect of sintering cracks on the erosion of EB-PVD TC is higher than that dominated by the temperature at the early stage of thermal cycles.

4.2.3. The Calculated Erosion Rate Versus Impact Angles under Different Ratios R_t

The erosion rates are also investigated versus impact angles at selected ratio R_t (Table 11). The calculated erosion rates are shown in Figure 19, with R_t from 0.2 to 0.67.

Table 11. Parameters used to calculate erosion rates versus impact angles at selected high-temperature dwell period and thermal cycles.

No# of Cycle	Temperatures (°C)	Impact Angles (°)	Impact Mass (kg)	Impact Velocity (m/s)	Ratio of R_t=t_{HIGH}/t_{cycle}
Determined cycle number N = 10,300	Randomly selected T ranging from [RT, 1400]	Determined impact angles α ranging from [5, 90]	Randomly selected m_i ranging from [0, M]	Determined V: 300	Determined R_t = 0.2, 0.67

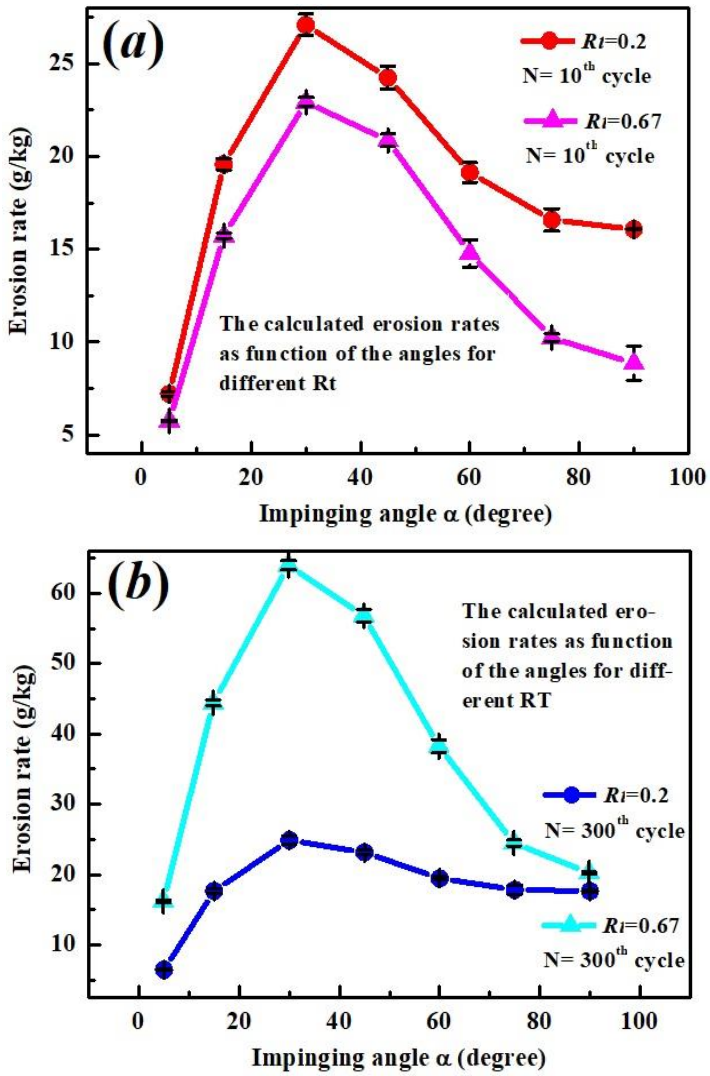

Figure 19. The calculated erosion rate versus impact angles with various ratios R_t at selected stages of thermal cycles; (**a**) N = 10; (**b**) N = 300.

Similar to the results from Figure 18, the temperature-dependent erosion behavior and sintering effect dominate at the early stages and at the late stages of thermal cycles, respectively. Pseudoductile erosion is found for the erosion curves, where the maximum erosion rates are identified at nearly 30° at either the earlier or later stages of thermal cycles.

5. Conclusions

A stochastic approach was combined with a mechanics-based erosion model to evaluate solid particle erosion behavior of EB-PVD TBCs under thermal cycling conditions. The results demonstrate that in addition to normal damage and degradation due to oxidation of bond coat under thermal cycling operation environments, the extrinsic damage due to solid particle erosion during thermal cycles needs thorough investigation, numerically. The present research achieves the following main results:

(1). For the silica particle–EB-PVD TBCs erosion system, the cutting wear and deformation wear kinetic energies can be evaluated using material properties of both erodent and target materials. A pseudoductile erosion behavior was identified at temperatures approximately above 220 °C. This behavior is attributed to an increased cutting wear at glancing impacting angles and to a decrease in deformation wear at high impacting angles due to the softening and/or partially molten silica particles at elevated temperatures.

(2). The erosion and erosion rate evaluated by using a stochastic approach was found to follow a normal distribution pattern with a mean value and standard deviation of $\mu \pm 2\sigma$. Additionally, it was identified that the erosion behavior of EB-PVD TBCs is dominated by either temperature at the early stages of thermal cycles or by the sintering at later stages of thermal cycles.

(3). The temperature-dependent erosion occurs, and the maximum erosion is achieved at low temperature in a brittle manner. For the isothermal furnace erosion test, there exists a significant sintering effect on the surface of the topcoat that could lead to extensive propagation of sintering cracks at deep depth within the topcoat. This potentially makes erosion occur at later stages of thermal cycles, and consequently produces considerable damage on the surface of the topcoat according to the estimated erosion (rates) for a large ratio of R_t. This facilitates the spallation of the topcoat and leads to catastrophic failure of EB-PVD TBCs.

Supplementary Materials: The following supporting information can be downloaded at: https://www.mdpi.com/article/10.3390/coatings13010156/s1, Figure S1: The calculated erosion rate of EB-PVD TC under impact of silica particles at RT.; Figure S2: The calculated erosion rate of EB-PVD TC under impact of alumina particles at 540 °C; Figure S3: The experimentally measured erosion rates at 910 °C with fitting curve used to obtain the cutting wear kinetic energy ϕ; Figure S4: The calculated erosion rate of EB-PVD TC under impact of silica particles at 910 °C. Figure S5: The calculated critical impact velocity of EB-PVD TC (**a**) as function of time for three cycles (**b**) as function of number of cycles; Figure S6: The schematic diagram of sintering crack developed within TC; Figure S7: Calculated critical through-thickness fracture toughness as function of crack length; Figure S8: Sintering crack length as function of high-temperature dwell time. Figure S9: Calculated erosion rates as a function of impact angles at first thermal cycle for different temperatures with erosion rates measured experimentally using (**a**) impact velocity 170 m/s (**b**) impact velocity 300 m/s; Figure S10: The calculated ratio of cutting wear over deformation wear as function of (**a**) different impinging angles and (**b**) various of temperatures; Figure S11: Calculated erosion as a function of high-temperature sintering time with erosion measured experimentally [10] for different accumulated mass (**a**) M = 0.5 g, (**b**) M = 0.8 g and (**c**) M = 1 g. Table S1: The experimentally measured erosion rate of EB-PVD TBCs; Table S2: Parameters used to calculate temperature-dependent fitting parameters; Table S3: Parameters of experimental settings in [11] used to calculate sintering-dependent fit-ting parameters. Table S4. Parameters of experimental settings in [14] used to calculate sintering-dependent fitting parameters.

Author Contributions: B.Z.: Conceptualization, Methodology, Validation, Investigation, Writing—original draft. K.C.: Conceptualization, Writing—review and editing, Supervision, Project administration, Resources, Funding acquisition. N.B.: Writing—review and editing, Supervision, Resources, Funding acquisition. All authors have read and agreed to the published version of the manuscript.

Funding: This research was supported by the Air Defence System Program of National Research Council Canada (DTS-NRC A1-018177). This work was also financially supported by the Natural Sciences and Engineering Research Council of Canada under grant number (RGPIN-2016-04190).

Institutional Review Board Statement: Not applicable.

Informed Consent Statement: Not applicable.

Data Availability Statement: Not applicable.

Acknowledgments: We acknowledgement the supports for this research by National Research Council Canada via DTS program and also by Natural Sciences and Engineering Research Council of Canada.

Conflicts of Interest: The authors declare no conflict of interest.

References

1. Strangman, T.; Raybould, D.; Jameel, A.; Baker, W. Damage mechanisms, life prediction, and development of EB-PVD thermal barrier coatings for turbine airfoils. *Surf. Coat. Technol.* **2007**, *202*, 658–664. [CrossRef]
2. Tolpygo, V.; Clarke, D.; Murphy, K. Oxidation-induced failure of EB-PVD thermal barrier coatings. *Surf. Coat. Technol.* **2001**, *146–147*, 124–131. [CrossRef]
3. Ozgurluk, Y.; Doleker, K.M.; Ozkan, D.; Ahlatci, H.; Karaoglanli, A.C. Cyclic Hot Corrosion Failure Behaviors of EB-PVD TBC Systems in the Presence of Sulfate and Vanadate Molten Salts. *Coatings* **2019**, *9*, 166. [CrossRef]
4. Zhang, B.; Chen, K.; Baddour, N.; Patnaik, P. Failure and life evaluation of EB-PVD thermal barrier coatings using temperature-process-dependent model parameters. *Corros. Sci.* **2019**, *156*, 1–9. [CrossRef]
5. Schulz, U.; Fritscher, K.; Ebach-Stahl, A. Cyclic behavior of EB-PVD thermal barrier coating systems with modified bond coats. *Surf. Coat. Technol.* **2008**, *203*, 449–455. [CrossRef]
6. Bhatnagar, H.; Ghosh, S.; Walter, M.E. Parametric studies of failure mechanisms in elastic EB-PVD thermal barrier coatings using FEM. *Int. J. Solids Struct.* **2006**, *43*, 4384–4406. [CrossRef]
7. Zhao, X.; Wang, X.; Xiao, P. Sintering and failure behaviour of EB-PVD thermal barrier coating after isothermal treatment. *Surf. Coat. Technol.* **2006**, *200*, 5946–5955. [CrossRef]
8. Courcier, C.; Maurel, V.; Rémy, L.; Quilici, S.; Rouzou, I.; Phelippeau, A. Interfacial damage based life model for EB-PVD thermal barrier coating. *Surf. Coat. Technol.* **2011**, *205*, 3763–3773. [CrossRef]
9. Wellman, R.; Nicholls, J. Some observations on erosion mechanisms of EB PVD TBCS. *Wear* **2000**, *242*, 89–96. [CrossRef]
10. Wellman, R.; Nicholls, J. A Monte Carlo model for predicting the erosion rate of EB PVD TBCs. *Wear* **2004**, *256*, 889–899. [CrossRef]
11. Wellman, R.; Nicholls, J. Erosion, corrosion and erosion–corrosion of EB PVD thermal barrier coatings. *Tribol. Int.* **2008**, *41*, 657–662. [CrossRef]
12. Wellman, R.; Deakin, M.; Nicholls, J. The effect of TBC morphology and aging on the erosion rate of EB-PVD TBCs. *Tribol. Int.* **2005**, *38*, 798–804. [CrossRef]
13. Chen, J.; Beake, B.D.; Wellman, R.G.; Nicholls, J.R.; Dong, H. An investigation into the correlation between nano-impact resistance and erosion performance of EB-PVD thermal barrier coatings on thermal ageing. *Surf. Coat. Technol.* **2012**, *206*, 4992–4998. [CrossRef]
14. Wellman, R.; Nicholls, J. On the effect of ageing on the erosion of EB-PVD TBCs. *Surf. Coat. Technol.* **2004**, *177–178*, 80–88. [CrossRef]
15. Busso, E.P.; Qian, Z.Q. A mechanistic study of microcracking in transversely isotropic ceramic–metal systems. *Acta Mater.* **2006**, *54*, 325–338. [CrossRef]
16. Schulz, U.; Saruhan, B.; Fritscher, K.; Leyens, C. Review on Advanced EB-PVD Ceramic Topcoats for TBC Applications. *Int. J. Appl. Ceram. Technol.* **2004**, *1*, 302–315. [CrossRef]
17. Nicholls, J.; Lawson, K.; Johnstone, A.; Rickerby, D. Methods to reduce the thermal conductivity of EB-PVD TBCs. *Surf. Coat. Technol.* **2002**, *151–152*, 383–391. [CrossRef]
18. Peters, M.; Leyens, C.; Schulz, U.; Kaysser, W.A. EB-PVD Thermal Barrier Coatings for Aeroengines and Gas Turbines. *Adv. Eng. Mater.* **2001**, *3*, 193–204. [CrossRef]
19. Renteria, A.F.; Saruhan, B.; Schulz, U.; Raetzer-Scheibe, H.-J.; Haug, J.; Wiedenmann, A. Effect of morphology on thermal conductivity of EB-PVD PYSZ TBCs. *Surf. Coat. Technol.* **2006**, *201*, 2611–2620. [CrossRef]

20. Wolfe, D.E.; Singh, J.; Miller, R.A.; Eldridge, J.I.; Zhu, D.-M. Tailored microstructure of EB-PVD 8YSZ thermal barrier coatings with low thermal conductivity and high thermal reflectivity for turbine applications. *Surf. Coat. Technol.* **2005**, *190*, 132–149. [CrossRef]
21. Nicholls, J.R.; Wellman, R.G.; Deakin, M.J. Erosion of thermal barrier coatings. *Mater. High Temp.* **2003**, *20*, 207–218. [CrossRef]
22. Nicholls, J.R.; Jaslier, Y.; Rickerby, D.S. Erosion of EB-PVD thermal barrier coatings. *Mater. High Temp.* **1998**, *15*, 15–22. [CrossRef]
23. Liu, Y.; Ravichandran, R.; Chen, K.; Patnaik, P. Application of Machine Learning to Solid Particle Erosion of APS-TBC and EB-PVD TBC at Elevated Temperatures. *Coatings* **2021**, *11*, 845. [CrossRef]
24. Fleck, N.; Zisis, T. The erosion of EB-PVD thermal barrier coatings: The competition between mechanisms. *Wear* **2010**, *268*, 1214–1224. [CrossRef]
25. Ning, S.; Yu, Q.; Liu, T.; Zhang, K.; Zhang, H.; Wang, Y.; Li, Z. Influence of particle shape on erosion behavior of EB-PVD thermal barrier coatings. *Ceram. Int.* **2022**, *48*, 8627–8640. [CrossRef]
26. Neilson, J.; Gilchrist, A. Erosion by a stream of solid particles. *Wear* **1968**, *11*, 111–122. [CrossRef]
27. Tabakoff, W. Investigation of coatings at high temperature for use in turbomachinery. *Surf. Coat. Technol.* **1989**, *39–40*, 97–115. [CrossRef]
28. Lakshmi, S.G.; Malvi, B.; Rao, D.S.; Das, D.K.; Roy, M. Comparison of erosion rate of EB-PVD and plasma sprayed TBC. *Surf. Eng.* **2021**, *37*, 1396–1403. [CrossRef]
29. Sheldon, G.; Kanhere, A. An investigation of impingement erosion using single particles. *Wear* **1972**, *21*, 195–209. [CrossRef]
30. Bitter, J. A study of erosion phenomena part I. *Wear* **1963**, *6*, 5–21. [CrossRef]
31. Evans, A.G.; Gulden, M.E.; Rosenblatt, M. Impact damage in brittle materials in the elastic-plastic response régime. *Proc. R. Soc. London. Ser. A, Math. Phys. Sci.* **1978**, *361*, 343–365. [CrossRef]
32. Slikkerveer, P.J. Mechanical Etching of Glass by Powder Blasting. Ph.D. Thesis, Technische Universiteit Eindhoven, Eindhoven, The Netherlands, 1999. [CrossRef]
33. Li, C.-J.; Dong, H.; Ding, H.; Yang, G.-J.; Li, C.-X. The Correlation of the TBC Lifetimes in Burner Cycling Test with Thermal Gradient and Furnace Isothermal Cycling Test by TGO Effects. *J. Therm. Spray Technol.* **2017**, *26*, 378–387. [CrossRef]
34. Gregorová, E.; Černý, M.; Pabst, W.; Esposito, L.; Zanelli, C.; Hamáček, J.; Kutzendörfer, J. Temperature dependence of Young's modulus of silica refractories. *Ceram. Int.* **2015**, *41*, 1129–1138. [CrossRef]
35. Dong, H.; Yang, G.-J.; Cai, H.-N.; Ding, H.; Li, C.-X.; Li, C.-J. The influence of temperature gradient across YSZ on thermal cyclic lifetime of plasma-sprayed thermal barrier coatings. *Ceram. Int.* **2015**, *41*, 11046–11056. [CrossRef]
36. Zhang, B.; Chen, K.; Baddour, N. Stress models for electron beam-physical vapor deposition thermal barrier coatings using temperature-process-dependent model parameters. *J. Eur. Ceram. Soc.* **2021**, *41*, 5658–5674. [CrossRef]
37. Zhang, B.; Chen, K.; Baddour, N. The Effect of Interfacial Roughness on Residual Stresses in Electron Beam-Physical Vapor Deposition of Thermal Barrier Coatings. *Coatings* **2021**, *11*, 341. [CrossRef]
38. Thompson, J.; Clyne, T. The effect of heat treatment on the stiffness of zirconia top coats in plasma-sprayed TBCs. *Acta Mater.* **2001**, *49*, 1565–1575. [CrossRef]
39. Busso, E.; Qian, Z.; Taylor, M.; Evans, H. The influence of bondcoat and topcoat mechanical properties on stress development in thermal barrier coating systems. *Acta Mater.* **2009**, *57*, 2349–2361. [CrossRef]
40. Guo, S.; Kagawa, Y. Effect of loading rate and holding time on hardness and Young's modulus of EB-PVD thermal barrier coating. *Surf. Coat. Technol.* **2004**, *182*, 92–100. [CrossRef]
41. Guo, S.; Kagawa, Y. Effect of thermal exposure on hardness and Young's modulus of EB-PVD yttria-partially-stabilized zirconia thermal barrier coatings. *Ceram. Int.* **2006**, *32*, 263–270. [CrossRef]
42. Zhu, J.; Ma, K. Microstructural and mechanical properties of thermal barrier coating at 1400 °C treatment. *Theor. Appl. Mech. Lett.* **2014**, *4*, 021008. [CrossRef]
43. Twigg, P.C.; Page, T.F. The temperature-variant hardness response of duplex TBCs. *Thin Solid Films* **1993**, *236*, 219–224. [CrossRef]
44. Evans, A.G.; Clarke, D.R.; Levi, C.G. The influence of oxides on the performance of advanced gas turbines. *J. Eur. Ceram. Soc.* **2008**, *28*, 1405–1419. [CrossRef]
45. Hutchinson, J.; Evans, A. On the delamination of thermal barrier coatings in a thermal gradient. *Surf. Coat. Technol.* **2002**, *149*, 179–184. [CrossRef]
46. Vaßen, R.; Giesen, S.; Stöver, D. Lifetime of Plasma-Sprayed Thermal Barrier Coatings: Comparison of Numerical and Experimental Results. *J. Therm. Spray Technol.* **2009**, *18*, 835–845. [CrossRef]
47. Du, Z.-Z.; Cocks, A. Constitutive models for the sintering of ceramic components—I. Material models. *Acta Met. et Mater.* **1992**, *40*, 1969–1979. [CrossRef]
48. Tsoga, A.; Nikolopoulos, P. Surface and grain-boundary energies in yttria-stabilized zirconia (YSZ-8 mol%). *J. Mater. Sci.* **1996**, *31*, 5409–5413. [CrossRef]
49. Cheng, B.; Zhang, Y.-M.; Yang, N.; Zhang, M.; Chen, L.; Yang, G.-J.; Li, C.-X.; Li, C.-J. Sintering-induced delamination of thermal barrier coatings by gradient thermal cyclic test. *J. Am. Ceram. Soc.* **2017**, *100*, 1820–1830. [CrossRef]
50. Goldsmith, A.; Hirschhorn, H.J.; Waterman, T.E. Ceramics. In *Handbook of Thermophysical Properties of Solid Materials*; Pergamon Press: Oxford, UK, 1961; Volume 3.
51. Simms, N.; Kilgallon, P.; Roach, C.; Oakey, J. Development of oxides at TBC—bond coat interfaces in burner rig exposures. *Mater. High Temp.* **2003**, *20*, 519–526. [CrossRef]

52. Beele, W.; Marijnissen, G.; van Lieshout, A. The evolution of thermal barrier coatings—status and upcoming solutions for today's key issues. *Surf. Coat. Technol.* **1999**, *120–121*, 61–67. [CrossRef]
53. Hodge, P.E.; Stecura, S.; Gedwill, M.A.; Zaplatynsky, I.; Levine, S.R. Thermal barrier coatings: Burner rig hot corrosion test results. *J. Mater. Energy Syst.* **1980**, *1*, 47–58. [CrossRef]
54. Kanwal, S.; Thakare, J.G.; Pandey, C.; Singh, I.; Mahapatra, M.M. Characterization of slurry-based mullite coating deposited on P91 steel welds. *J. Aust. Ceram. Soc.* **2019**, *55*, 519–528. [CrossRef]
55. Thakare, J.; Pandey, C.; Mulik, R.; Mahapatra, M. Mechanical property evaluation of carbon nanotubes reinforced plasma sprayed YSZ-alumina composite coating. *Ceram. Int.* **2018**, *44*, 6980–6989. [CrossRef]